Recent advances in zinc ferrite (ZnFe2O4) based nanostructures for magnetic hyperthermia applications

Journal:	*ChemComm*
Manuscript ID	CC-FEA-04-2023-001637.R1
Article Type:	Highlight

SCHOLARONE™
Manuscripts

Recent advances in zinc ferrite (ZnFe2O4) based nanostructures for magnetic hyperthermia applications

Priyambada Sahoo[1#], Piyush Choudhary[1#], Suvra S. Laha[2], Ambesh Dixit[1], O. Thompson Mefford[2]*

1. Advanced Materials and Devices (A-MAD) Laboratory, Department of Physics, Indian Institute of Technology (IIT) Jodhpur, Karwar, Jodhpur, Rajasthan, 342030, INDIA,
* Corresponding author: Email:ambesh@iitj.ac.in
2. Department of Materials Science & Engineering, Clemson University, Clemson, SC 29634, USA,
* Corresponding author: Email:mefford@clemson.edu
 # These authors contributed equally to this work

Recent advances in zinc ferrite (ZnFe₂O₄) based nanostructures for magnetic hyperthermia applications

Priyambada Sahoo[1#], Piyush Choudhary[1#], Suvra S. Laha[2], Ambesh Dixit[1]*, O. Thompson Mefford[2]*

Spinel ferrite-based magnetic nanomaterials have been investigated for numerous biomedical applications, including targeted drug delivery, magnetic hyperthermia therapy (MHT), magnetic resonance imaging (MRI), and biosensors, among others. Recent studies have found that zinc ferrite-based nanomaterials are favorable candidates for cancer theranostics, particularly for magnetic hyperthermia applications. Zinc ferrite exhibits excellent biocompatibility, minimal toxicity, and more importantly, exciting magnetic properties. In addition, these materials demonstrate a Curie temperature much lower than other transition metal ferrites. By regulating synthesis protocols and/or introducing suitable dopants, the Curie temperature of zinc ferrite-based nanosystems can be tailored to the MHT therapeutic window, i.e., 43 - 46 ℃, a range which is highly beneficial for clinical hyperthermia applications. Furthermore, zinc ferrite-based nanostructures have been extensively used in successful pre-clinical trials on mice models focusing on the synergistic killing of cancer cells involving magnetic hyperthermia and chemotherapy. This review provides a systematic and comprehensive understanding of the recent developments of zinc ferrite-based nanomaterials, including doped particles, shape-modified structures, and composites for magnetic hyperthermia applications. In addition, future research prospects involving pure ZnFe₂O₄ and its derivative nanostructures have also been proposed.

1. Introduction

Magnetic nanoparticle hyperthermia has been proven to be a promising technology in the advancement of cancer nanomedicine research. In a typical magnetic hyperthermia therapy (MHT) procedure, localized heat is generated by magnetic nanoparticles in the presence of an alternating magnetic field (AMF) at high frequencies (*i.e.*, hundreds of kHz).[1–4] The heat produced during MHT primarily results from two fundamental nanomagnetic phenomena, namely, the Néel and Brownian relaxations. The Brownian relaxation time depends on the physical rotation of the entire particle in the fluid medium, whereas the Néel relaxation is determined by the intrinsic electronic spin rotation inside the particle. In the physiological domain, the motion of the particles may potentially be limited due to cellular interactions. In this case, the Néel mechanism will be the dominant mode of relaxation. Past research has demonstrated that heat emanating during MHT carries the potency to destroy both cancer and bacteria cells.[1–10] Despite proposed by Gilchrist and co-workers as early as in 1957, [11] the underlying mechanism of how a malignant cell succumbs during MHT remains a debatable subject that needs

further investigation. The role of crucial biochemical factors like heat-shock proteins, DNA alterations, and other enzymatic processes that initiate during a typical MHT need to be more carefully understood before commenting on hyperthermia-induced cell death.[12–16] The key parameters that determine nanoparticle heating during MHT include shape, size, saturation magnetization (M_s), coating material, and concentration of nanoparticles, among other.[17–23]

This procedure, which is primarily non-invasive and, thus, has attracted scientists to further advance this research domain, has the potential to modernize future nanomedicine research. In the past two decades, MHT has attracted significant attention because of its ability to destroy malignant tumors when practiced concurrently with traditional chemo and radiotherapy strategies. This synergistic approach of combining MHT with other advanced therapies has dominated the cancer nanomedicine research over the few years.[24–26] In Europe, MHT has been practiced as an adjuvant therapy to treat human glioblastoma, an aggressive form of brain cancer, in conjunction with radiotherapy.[27,28] Currently, dedicated attempts are focused on designing and developing smart nanomaterials based on superparamagnetic spinel ferrites for the advancement of MHT treatment procedure.[29–32] Among the several multi-functional spinel ferrites, zinc ferrite (ZnFe₂O₄) deserves special attention because it exhibits excellent biocompatibility,[33] minimal toxicity and, more importantly, exciting magnetic properties[34] as well as Curie temperatures lower than other ferrites.[35,36] In a typical MHT procedure, the therapeutic temperature window falls somewhere between ~43−46 ℃.[33] At this temperature range, the cancer cells

1. Advanced Materials and Devices (A-MAD) Laboratory, Department of Physics, Indian Institute of Technology (IIT) Jodhpur, Karwar, Jodhpur, Rajasthan, 342030, INDIA,
* Corresponding author: Email:ambesh@iitj.ac.in
2. Department of Materials Science & Engineering, Clemson University, Clemson, SC 29634, USA,
* Corresponding author: Email:mefford@clemson.edu Address here.
# These authors contributed equally to this work

succumb leaving the healthy ones unaffected. However, sustaining this brief temperature window for the time needed (i.e., 30-60 minutes), particularly for clinical hyperthermia applications, is challenging. Bulk zinc ferrite is antiferromagnetic in nature having a Néel temperature as low as 10 K;[37] however, in the nano domain it exhibits substantial saturation magnetization, and more importantly, a magnetic transition temperature in tens of Kelvin, which is significantly lower compared to other ferrites. For example, Fe_3O_4 (T_c~855 K)[38], $MnFe_2O_4$ (~580 K)[23] and $CoFe_2O_4$ (793 K)[40] report higher Curie/Néel temperatures than $ZnFe_2O_4$. By tuning synthesis protocols and/or introducing suitable dopants, the Curie/Néel temperature of zinc ferrite-based nano systems can be tailored to the MHT therapeutic window range, providing zinc ferrite-based nano systems a self-regulated temperature or a controlled heating in the 43−46 °C range, making them unique ferrite material for clinical magnetic hyperthermia applications.[41–43]

Magnetite (Fe_3O_4) exhibits an inverse spinel structure with the tetrahedral A sites occupied only by Fe^{3+} ions and the octahedral B sites inhabited alternatively by Fe^{2+} and Fe^{3+} ions.[30] Interestingly, the magnetic moment contribution in bulk magnetite comes primarily from the Fe^{2+} ions because the Fe^{3+} ions in both sites are directly opposite from each other effectively canceling their moments as illustrated in **Figure 1A**. However, $ZnFe_2O_4$ exhibits a normal spinel configuration with A and B sites occupied by Zn^{2+} and Fe^{3+} ions, respectively (**Figure 1B**). From **Figure 1B**, it is observed that the magnetic moment contribution from the Fe^{3+} ions in the B site boils down to zero., However, Zn^{2+}, being paramagnetic in nature (filled d-orbitals), in the bulk form, zinc ferrite ($ZnFe_2O_4$) exhibits antiferromagnetic behavior (~ zero magnetic moment).
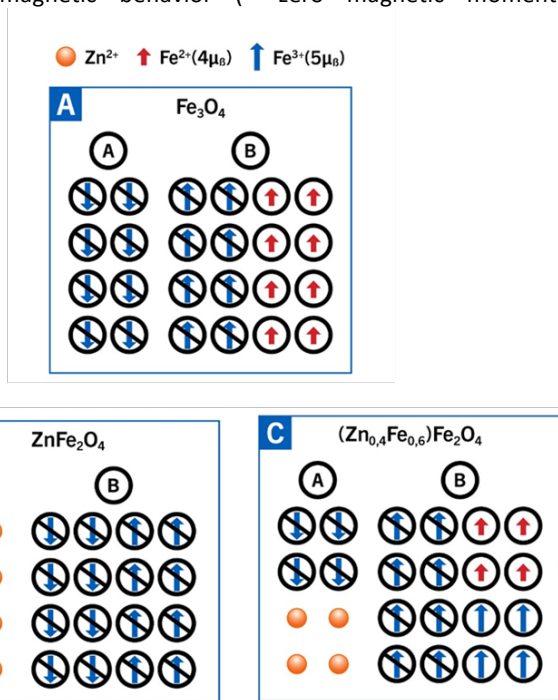
Figure 1. Schematic representation of A (tetrahedral) and B (octahedral) magnetite sites with zinc doping.

Surprisingly, the zinc ferrite based nanosystems show substantial saturation magnetization (M_s) near room temperature, sometimes as high as ~ 90 emu/g depending on doping percentage, functionalization, morphology and synthesis protocol.[33,44,45] Therefore, the question remains how antiferromagnetic material in bulk form can display such a high magnitude of M_s in the nano domain. The most prominent factor contributing to the magnetic moment of nano zinc ferrite could possibly be a disordered arrangement of Fe^{3+} spins in both A and B sites or only in B sites in a manner such that the effective moments do not oppose each other. Furthermore, the spin-canting effect observed in nanoparticles also contributes to the higher magnetic moment of zinc ferrite.

Doping is an important phenomenon by which one can obtain zinc ferrite-based nano systems with significantly greater magnetic moments and potentially a higher thermal energy conversion. Once zinc ferrite is doped with other ions, in particular magnetically relevant ions like Ni^{2+}, Co^{2+}, and Mn^{2+}, among others, the positioning of the ions in the spinel system is altered, effectively contributing to a non-zero magnetic moment as depicted in **Figure 1C** for a $(Zn_{0.4}Fe_{0.6})Fe_2O_4$ spinel configuration. Furthermore, the transition metal zinc records a minimum toxicity level as opposed to ions like cobalt. Additionally, $ZnFe_2O_4$ and its associated nanostructures exhibit substantial specific absorption rate (SAR) values. SAR, which gives a quantitative measurement of the heat generated by the particles during MHT, is expressed by the mathematical formula

$$SAR = \frac{dT}{dt} \times C_p \times \frac{m_s}{m_n}$$

where C_p denotes the specific heat of the solution, m_s represents the mass of the suspension, m_n represents the mass of the nanoparticles, and $\frac{dT}{dt}$ represents the initial slope of the heating curve. The SAR is expressed in W/g.[30]

Currently, the number of detailed review articles available on zinc ferrite in the scientific literature,[46,47] is limited, substantiating the need to review $ZnFe_2O_4$-based nanostructures for advanced biomedical applications. In this review, comprehensive details focusing on the magnetic hyperthermic potential of $ZnFe_2O_4$ and its derivative nanomaterials including doped, shape anisotropic systems and composites are presented. This review is primarily aimed at investigating the hyperthermia performance of zinc ferrite-based nanosystems by analyzing their various synthesis approaches, morphological modifications, doping strategies, heat profiles, and cell viability studies. The authors conclude with future research possibilities and applications focusing on various aspects of $ZnFe_2O_4$ based nanostructures.

2. Synthesis of zinc ferrite nanostructures

In nanomaterial applications, the synthesis strategies carry enormous importance. The properties of the nanostructures are highly dependent upon the chosen method of fabrication. Several methods have been developed to produce spherical ZFNPs including combustion,[48] hydrothermal,[44,49,50] co-precipitation,[22,23,44] thermal decomposition,[51,52] and biological synthesis methods,[53–55] as summarized in **Figure 2**.

ARTICLE
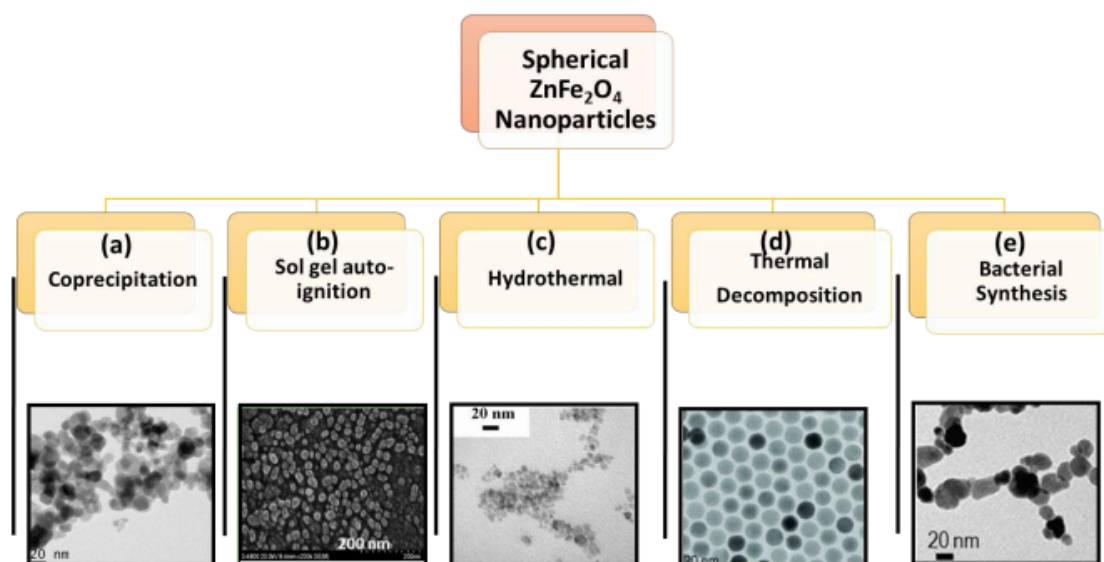
Figure 2. Electron microscopic images of spherical ZFNPs obtained using various synthesis approaches. The commonly used fabrication methods include (a) co-precipitation, (Reproduced with permission from ref.[56]. Copyright 2022, ELSEVIER). (b) sol gel auto-ignition or combustion synthesis, (Reproduced with permission from ref.[36]. Copyright 2020, ELSEVIER). (c) hydrothermal synthesis, (Reproduced with permission from ref.[50]. Copyright 2012, ELSEVIER) (d) thermal decomposition (Reproduced with permission from ref.[51]. Copyright 2009, WILEY) and (e) bacterial synthesis (Reproduced with permission from ref.[54]. Copyright 2014, Royal Society of Chemistry).

These methods and their parameters for synthesis have a decisive impact on properties such as the shape, size, and morphology of the ZFNPs. These, in turn, are responsible for properties (saturation magnetization, super-paramagnetism, magnetic anisotropy etc.,) relevant in the context of magnetic hyperthermia. We will briefly look at the synthesis methods for ZFNPs. The co-precipitation method is one of the most common and simplistic methods used for the synthesis of ferrite nanoparticles.[22,56–61] It is similarly translated to ZFNPs as well as it is one of the easiest and most cost-effective methods for their synthesis. As its name indicates, this process usually involves the simultaneous precipitation of soluble salts of the two cationic components in the ZFNPs, often achieved by creating a highly alkaline environment in the reaction medium (pH ~11-12). Frequently, the pH is the critical parameter in these synthesis procedures.[62,63] Nguyen et al.[62] have reported a critical analysis of the pH during the precipitation of ZFNPs. However, agglomeration as well as the large particle size distribution and large particle size (> 20 nm) of the ZFNPs formed through co-precipitation are several of the major drawbacks to this method. Efforts have been made to improve both particle size distribution and agglomeration by implementing various surfactants such as PVA, PVP, PEG, and Glycerol, among others.[64,65]

Another simple method for ZFNP synthesis, the combustion method,[36,66–70] typically involves formation of a gel of the desired ratio of precursors in the presence of a mild reducing agent, with citric acid being the most frequently used. This gel is combusted into ashes at an appropriate temperature. The temperature of combustion and calcination after combustion are often the determining parameters for this synthesis. While this method is known for its simplicity and minimal use of toxic chemicals, its disadvantages include high operation temperature, large particle size distribution, and high agglomeration, among others.

The disadvantages of the co-precipitation and the combustion method can be improved by other synthesis methods, one such method for ZFNP synthesis being thermal decomposition (TD).[71–78] In this synthesis, a metallic complex is thermally decomposed by dissolving it in an organic solvent with a high boiling point. These decomposed intermediates then stabilize in the form of NPs. To control the size of these NPs, a surfactant or ligand is usually added during the synthesis. The TD method is known for synthesis of anisotropic nanoparticles, with accurate size control, very fine size distribution and little agglomeration being the signature features of this method as they are the important properties required in the design of hyperthermia agents. The major disadvantages of this method are the use of organic solvents

and reagents, both of which are highly toxic. The hyperthermia application requires the preparation of ferrofluid in saline stable colloidal solutions. However, Rubio et al.[71] proposed a procedure to stabilize the NPs in aqueous colloidal solutions. The hydrothermal method, another controlled method used for the synthesis of ZFNPs,[79–83] involves the treatment of inorganic salts in water under high pressure. The temperature and time are the important reaction parameters that can be used to critically control the properties of the ZFNPs.[80,81] This method is typically known for producing small uniform ZFNPs of high purity and crystallinity. While it is perhaps one of the best methods for synthesis, the high reaction temperatures and long reaction times are a concern for this method. In addition, the

yield when synthesizing in large quantities is also not good, which is the most important drawback to this synthesis pathway.

Representative transmission electron microscopy (TEM) images of spherical ZFNPs that have been utilized in magnetic field-mediated hyperthermia are shown in **Figure 2,** with **Table 1** providing a brief overview of the comparative quality of spherical ZFNPs prepared using different synthesis protocols. Advancements in fabrication methods have led to improved dispersion and uniformity of the nanoparticles produced, resulting in better hyperthermia performance.

Table 1. Properties of nano zinc ferrites for magnetic hyperthermia applications produced using different synthesis techniques.

Synthesis Method	Process Parameters		Particle Size	Particle Size Distribution	Shape Control	Yield
	Precursors	Reaction Temperature				
Co-Precipitation	Inorganic salts in water	Low	~ 30 nm	Broad	Small	Good
Hydrothermal	Inorganic salts dissolved in water	High	< 20 nm	Monodisperse	Good	Average
Thermal Decomposition	Metal complexes in organic solvents	High	< 20 nm	Very Narrow	Very High	Average
Combustion	Inorganic salts and chelating agents in water	Very High	> 50 nm	Polydisperse	Very Little	Good
Biological Synthesis	Biological reducing and capping agents with inorganic salts in water	Low	~ 50 nm	Very Broad	Very Little	Average

3. Performance evaluation parameters of zinc ferrite-based nanoparticles for magnetic hyperthermia applications

The performance factor is primarily determined by three important characteristics, namely, 1. a substantial high saturation magnetization (M_S) of ZFNPs; 2. a high specific absorption rate (SAR) or specific loss power (SLP) of the ZFNP-based ferrofluid; and 3. superior cell viability performance when incubated with these nanoparticles.

3.1. High Saturation Magnetization (M_S): The saturation magnetization for ZFNPs is observed to be approximately 35-40 emu/g in the nanoparticle diameter range of 15-50 nm. However, this improved synthesis control has led to the efficient production of extremely small nanoparticles, which are superparamagnetic in nature and exhibit a higher saturation magnetization.[36,84] Although discussion of the factors influencing saturation magnetization is beyond the objective of this review, the highest saturation magnetization achieved by ZFNPs is reported to be 90.23 emu/g, achieved by a two-step co-precipitation technique followed by a microwave-assisted hydrothermal method (**Figure 3. (a)**).[44]

3.2. Specific Absorption Rate (SAR): SAR is an important parameter for analyzing the hyperthermia performance of magnetic nanoparticles. Typically, the SAR values for ZFNP-based ferrofluids lie above 100 W/g. For example, Somvanshi et al.[36] reported SAR values decreasing as the concentration of ZFNPs in the ferrofluid increased (**Figure. 3 (b)**), suggesting the impact of interparticle interactions on the resulting SAR value. Currently, maximizing the SAR output is one of the primary goals in designing an appropriate hyperthermia agent, and ZFNP-based ferrofluids have established themselves as a prime candidate in this regard. The details concerning particle size, morphology, surface functionalization, saturation magnetization, and SAR values obtained from some of the recent studies are reported in **Table 3**.

3.3. Cytotoxicity and Cell viability: The third critical parameter in determining hyperthermia efficiency is the cytotoxicity of the nanoparticles. Zinc is an important transition metal ion, the concentration of which in the human body is critical. Research has found that a deficiency of zinc leads to carcinogenic malformations.[85] In addition, the toxicity level of zinc is substantially lower compared to other elements used in doping

ARTICLE
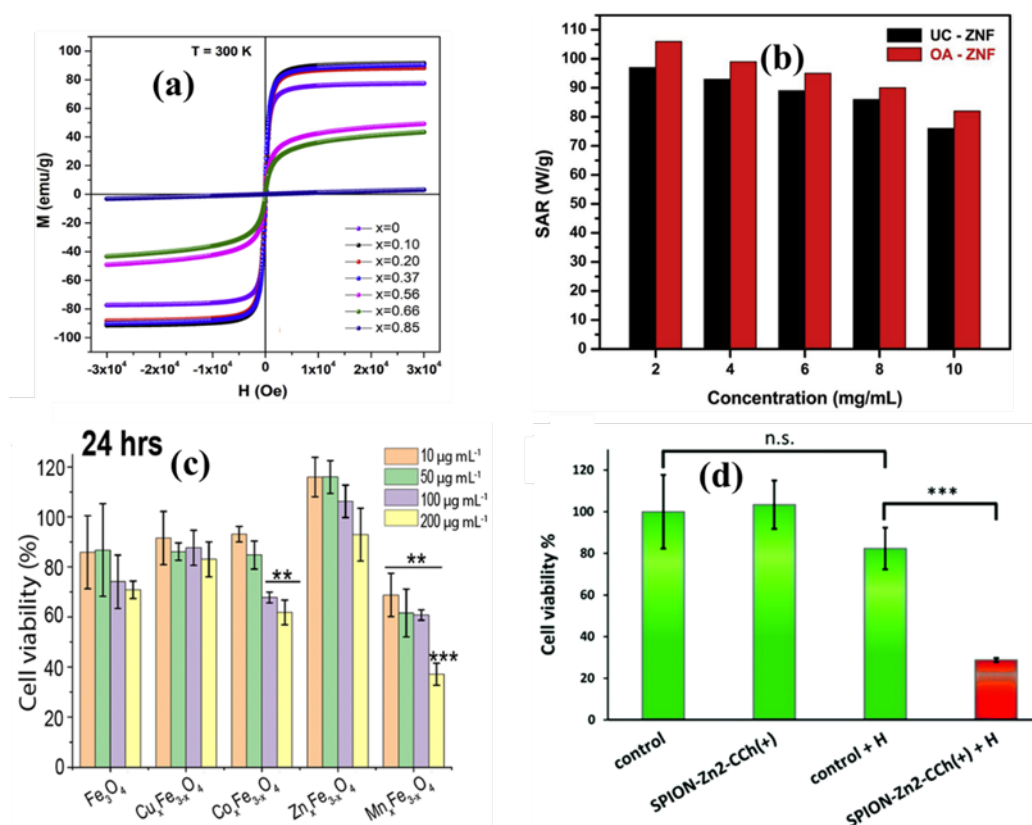
Figure 3. (a) The plot presenting saturation magnetization of varying ZFNPs (Reproduced with permission from ref.[44]. Copyright 2019, ELSEVIER). (b) The bar graph representing variation of SAR with respect to nanoparticle concentration in the ferrofluid used in a typical hyperthermia experiment where UC-ZNF refers to uncoated zinc ferrite NPs and OA-ZFNPs refers to Oleic Acid Capped zinc ferrite NPs. (Reproduced with permission from ref.[36]. Copyright 2020, ELSEVIER). (c) Effect of doped ferrite nanoparticles on viability of A549 cells after 24 h of exposure, calculated as fold changes compared with the control. The statistical analysis was performed with respect to the control. (Reproduced with permission from ref.[87]. Copyright 2019, Royal Society of Chemistry). (d) The cell viability plot showing a significant reduction in the percentage cell viability of cancer cell line (marked with the red bar) when exposed to magnetic hyperthermia using ZFNPs (Reproduced with permission from ref.[33]. Copyright 2019, Royal Society of Chemistry).

magnetic ferrites such as Mn, Co, and Ni. ZFNPs have shown great promise, becoming a recent trend in hyperthermia material due to their cytotoxic properties. They have an advantage over other doped ferrites due to the high dosage limit[86] of Zn^{+2} ions in the human body along with their antifungal and antibacterial properties.[66] A recent study conducted by S. Chakroborty et al.[87] shows the relative cytotoxicity of various doped ferrites on the human lung epithelial cell line (A549). Their study focused on various factors affecting the cytotoxicity of doped ferrites, specifically Cu, Co, Mn, and Zn. Of these Zn and Cu doped ferrites were observed to exhibit superior cytotoxic behavior. **Figure 3. (c)** shows the cell viability of the various doped ferrites studied at the exposure of 24 hrs where

Zn doped ferrite is seen as clearly performing better than the others. This result is supported by the study conducted by Lachowicz et al.[17], who applied a special coating of biocompatible polysaccharide that improved the cytotoxic behavior even further. **Figure 3. (d)** shows, the cell viability of the cancer cell line is shown to be perfectly intact in the presence of ZFNPs. However, with the hyperthermia treatment the cell viability exhibits a drastic reduction. These are clear indications that zinc doped ferrites are better candidates than conventional ferrites in this case. In addition, it was found that $Zn_xFe_{3-x}O_4$ cytotoxicity was largely dependent on the dissolved ions. **Table 2** shows the cytotoxic values in percentages due to the dissolved ions of various doped ferrites over different time periods of exposure.

ARTICLE

Table 2. Summary of the cytotoxicity of various doped ferrites commonly used in magnetic hyperthermia applications (Reproduced with permission from ref.[85]. Copyright 2019, Royal Society of Chemistry).

Sl. No.	Ferrite composition	Toxicity through dissolved ions (%)		
		24 hrs	48 hrs	72 hrs
1	$CuFe_2O_4$	8.8	26.9	34.6
2	$MnFe_2O_4$	15.5	22.1	29.6
3	$CoFe_2O_4$	12.2	24.1	29.6
4	$ZnFe_2O_4$	9.2	17.7	27.6

4. Undoped zinc ferrite-based nanostructures for MHT applications

This section highlights the recent achievements of undoped zinc ferrite nanomaterials (i.e., those consisting of only Zn and Fe) exhibiting various morphologies aimed at magnetic hyperthermia applications. The spherical zinc ferrite nanoparticles (ZFNPs) are perhaps the most studied and widely utilized forms in MHT. However, recently shape anisotropic nanoparticles have also shown great promise in this regard. We now consider more fully a few of the recent articles in this domain to investigate the factors involved in improved hyperthermia performance.
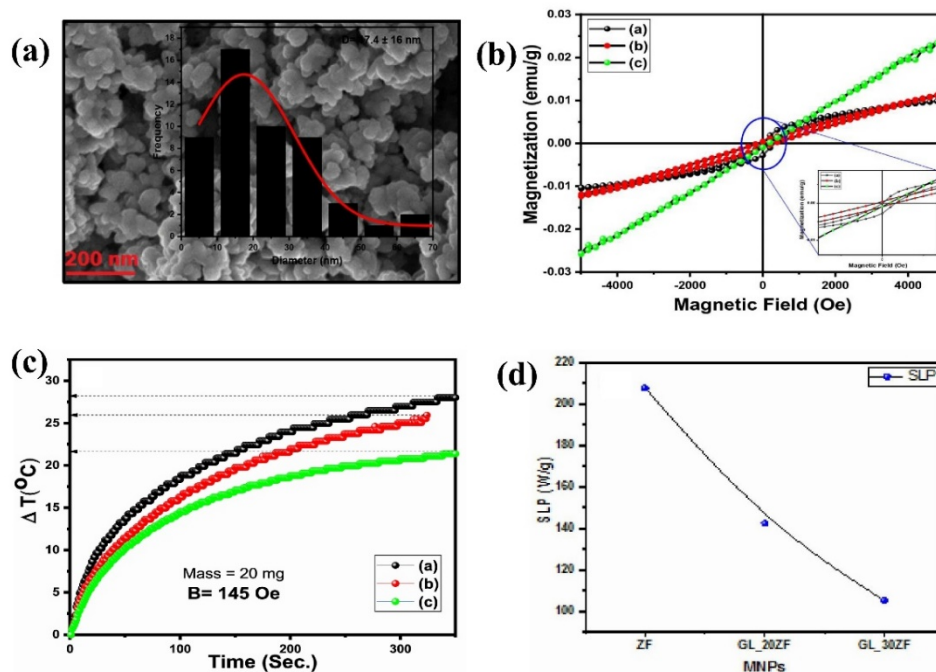
Figure 4. (a) SEM image of the uncoated ZFNPs produced using a green synthesis method. (b) Magnetization curves for the ZFNPs under an applied magnetic field. The uncoated ZFNPs, 20 ml leaf extract coated ZFNPs and 30 ml leaf extract coated ZFNPs are shown in black, red, and green colored curves respectively. (c) The time dependent relative increasing temperature plot for the ZFNP magneto-fluid. The uncoated ZFNPs, 20 ml leaf extract coated ZFNPs and 30 ml leaf extract coated ZFNPs are shown in black, red, and green colored curves respectively. (d) The variation of the SLP based on the concentration of the coating agent used (Reproduced with permission from ref. [53]. Copyright 2022, Springer).

ARTICLE

4.1. Spherical zinc ferrites: In this section, we will have a closer look at a few of the most interesting studies during recent times conducted on spherical ZFNP systems. One of the most recent studies conducted by Onyedikachi et al.[53] used a green route in the synthesis of ZFNPs. Specifically, Gongronema Latifolium leaf extract was used as both the reducing and the coating agent for the synthesis of these nanoparticles (**Figure 4. (a)**). The saturation magnetization of these nanoparticles increased with increasing amounts of the capping agent, i. e., the leaf extract (**Figure 4. (b)**). The saturation magnetization of these nanoparticles was found to be relatively lower compared to others reported in literature. However, the magnetic fluid prepared using these nanoparticles showed a satisfactory hyperthermia response, with SLP values ranging from 100-220 W/g. The t_{42} parameter, the time taken to reach 42 ℃ in the presence of AMF during magnetic hyperthermia from the room temperature, in this study for the 20 ml capped ZFNPs was found to be approximately 2-3 minutes, and the fluid reached saturation within five minutes of the experiment (**Figure 4(c)**). The SLP reported for this magneto-fluid was 142.6 W/g. A plot depicting the variation of SLP with the capping agent used is shown in **Figure 4. (d)**. As this plot indicates, the SLP was reduced with the increase in the capping agent used at the time of synthesis. A second recent study conducted by Vijaykanth et al. [88] explored producing ZFNPs via the solvothermal reflux method; the resulting SEM image is shown in **Figure 5. (a)**. In this study, zwitterionic dopamine sulphate ligands were used as surfactants for capping the ZFNPs, with the results finding that this coating is one of the most effective as it significantly enhances their saturation magnetization as can be seen by comparing the graphs in **Figure 5. (b)** and **(c)**. The investigation of hyperthermia performance was conducted using nanoparticle fluids of concentrations 1 mg/ml and 3 mg/ml (**(Figure 5 (d)**). The t_{42} was reported to be approximately 2 minutes under the influence of a magnetic field of 35.33 kA/m at 315 kHz. The magnitude of SAR was relatively higher (~ 393 W/g) under these magnetic field conditions and with a magnetic nanoparticle concentration of 3 mg/ml. This SAR value is one of the highest recently reported for spherical ZFNPs. Another interesting recent work on spherical ZFNPs was conducted by Somvanshi et al.[36] where oleic acid capped spherical ZFNPs were produced using a sol-
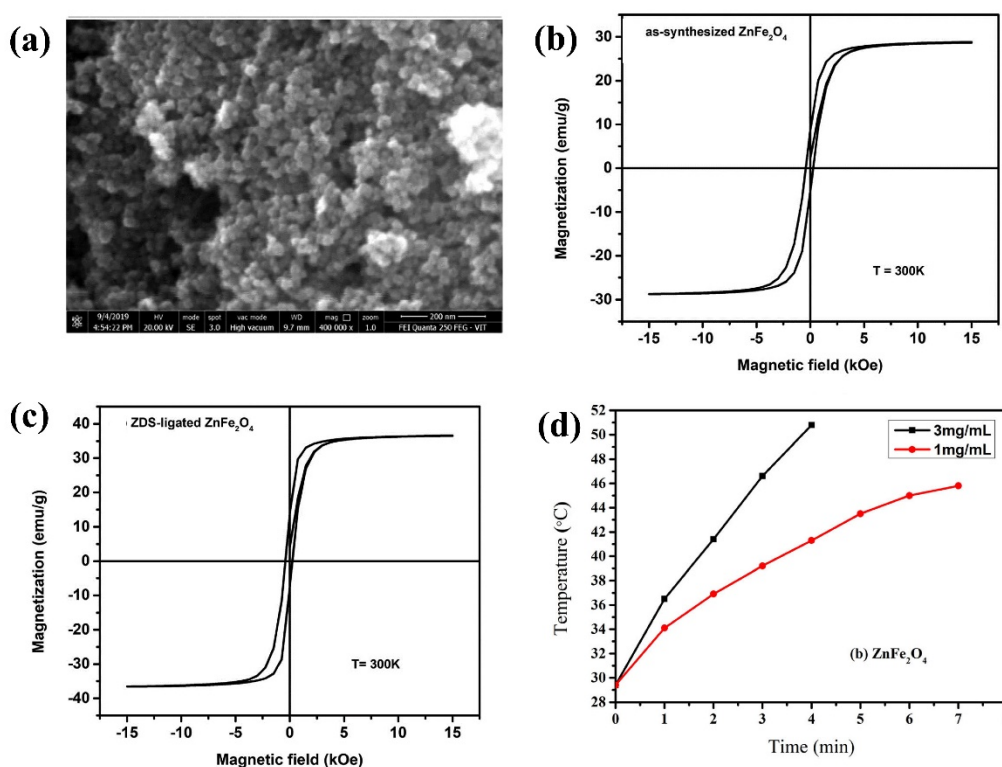
Figure 5. (a) SEM image of the ZFNPs produced using the solvothermal reflux method. (b) Magnetization curve for uncoated ZFNPs. (c) Magnetization curve after coating with a dopamine derivative. (d) The time dependent temperature rise plot for the magnetic fluids prepared by using the dopamine derivative coated ZFNPs at concentrations 1 and 3 mg/ml. (Reproduced with permission from ref.[88]. Copyright 2021, Springer).

ARTICLE
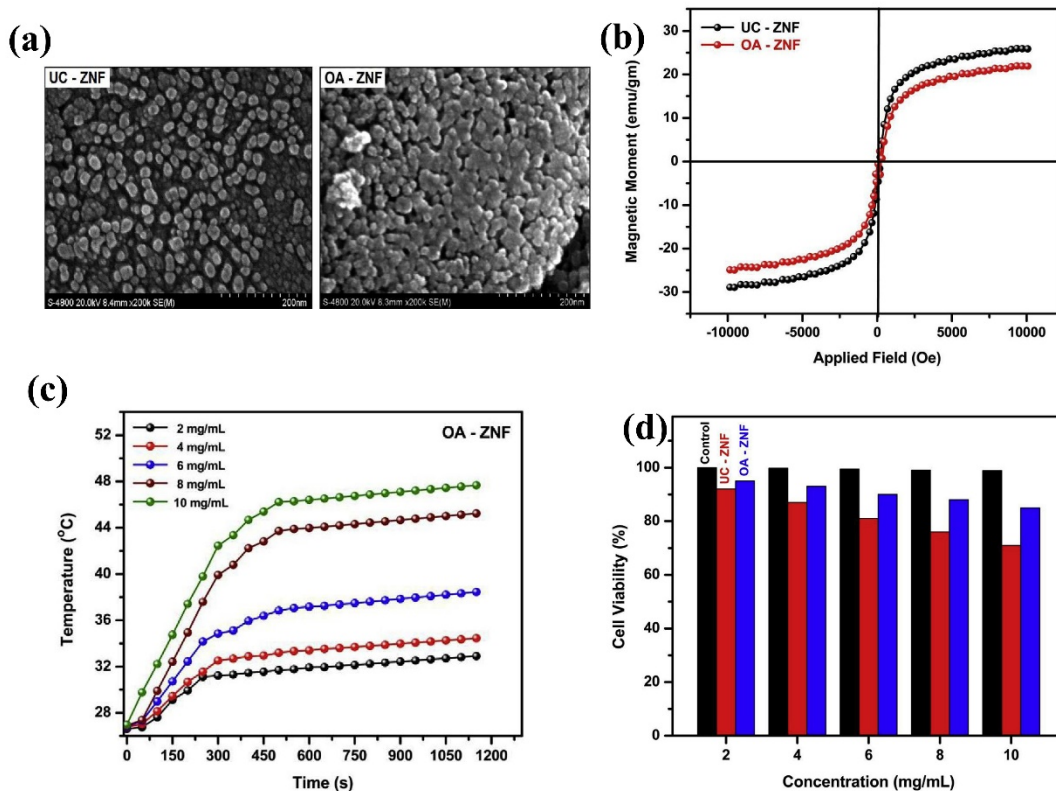
Figure 6. (a) SEM images of the uncoated and oleic acid (OA) coated ZFNPs produced using an auto-ignition process. (b) The plot of magnetic moment corresponding to the applied magnetic field for uncoated and OA coated ZFNPs. (c) The temperature increase of the magnetic nanoparticle fluid using various concentrations of ZFNPs with respect to time. (d) The cell viability plot showing the percentage cell viability when cell lines were incubated using ZFNP fluids of various concentrations. (Reproduced with permission from ref.[36]. Copyright 2020, ELSEVIER).

gel auto ignition route. The SEM image of these nanoparticles can be seen in **Figure 6. (a)**. Of particular interest here is the capping of ZFNPs by oleic acid renders their surfaces hydrophilic in nature, enabling the easy dispersion of these nanoparticles in water. The capped nanoparticles exhibit a magnetic saturation of 23.59 emu/g at room temperature. The plot of the magnetic moment with respect to the magnetic field applied is shown in **Figure 6. (b)**. In this study, magnetic-induced heating of zinc ferrite ferrofluid was performed using concentrations of ZFNPs varying from 2 mg/ml to 10 mg/ml, with the best results being obtained using the 10 mg/ml concentration fluid. The temperature increase observed over time is shown in **Figure 6. (c),** with the t_{42} being achieved in less than 5 minutes. During this magnetic heating process, the magnetic field was 35 kA/m at 350 kHz. The SAR value obtained was 105 W/g for the 2 mg/ml fluid under these magnetic field conditions. The cytotoxicity tests were conducted by incubating the cell lines for 2

days, with the results showing more than 70 % cell viability in all the cases. The plot of cell viability with respect to incubations with various concentrations of nanoparticle fluid is shown in **Figure 6. (d)**. As expected, the cells coated with nanoparticle fluid showed significantly better viability than the uncoated ones.

4.2. Shape anisotropic zinc ferrites

Spherical nanoparticles have shown much promise, the use of anisotropic particles having cubic and polyhedral morphologies has opened new avenues for enhancement of hyperthermia properties. These anisotropic ZFNPs typically exhibit higher saturation magnetization and SAR values than their spherical counterparts as it is evident from **Table 3.** Research efforts in nanoparticle morphology-based hyperthermia has seen increasing interest recently. To evaluate the performance of these ZFNPs, we review a few recently published articles on anisotropic ZFNPs. One of the most recent works in this areas has been reported by Shatooti *et al*.[45], who synthesized ZFNPs of various compositions using the chemical co-

ARTICLE

precipitation method. The capping agents used in this research were citric acid and Pluronic-F127, with the resulting product having a cubical morphology. The TEM image of the produced ZFNPs is shown in **Figure 7. (a).** These particles had an average dimension of 35-40 nm, and the maximum saturation magnetization of the ZFNPs was reported to be 95.2 emu/g (**Figure 7. (b)**) with a composition of $Zn_{0.1}Fe_{2.9}O_4$, a significantly higher value than typically obtained from most spherical zinc ferrite systems. The hyperthermia studies on the ferrofluid prepared using these ZFNPs were conducted using concentrations varying between 1.26 mg/mL and 10.57 mg/ml. The ferrofluid at a concentration of 1.26 mg/ml could not achieve an appropriate hyperthermia temperature (~ 42-46 °C). The plot of the temperature increase with respect to time is shown in **Figure 7. (c)**.

Another important study was conducted by Pardo *et al.*[89], who synthesized nanoparticles using a thermal decomposition method. The TEM image of the ZFNPs produced by this method is shown in

As this graph shows, the ferrofluid with a concentration of 10.57 mg/ml resulted in a temperature increase that crossed the hyperthermia therapeutic window. Thus, an intermediate concentration may be ideal for hyperthermia applications. The SAR value reported was the highest for the 1.26 mg/ml ferrofluid with a numerical value of 539 W/g. This value dropped to 161 W/g for the 10.57 mg/mL ferrofluid. The thermal stability studies performed on these NPs used thermogravimetric analysis (TGA), the results finding that these NPs were essentially stable up to 600 °C. **Figure 7. (d)** shows the TGA response of the ZFNPs. This plot shows a loss of mass initially that is determined to have been caused by the evaporation of the water absorbed, indicating that the nanoparticles do not lose mass easily and have excellent thermal stability.

Figure 8. (a). The particles of various sizes seen here were obtained by tuning the amount of the metallic precursors and the reaction time. The saturation magnetization plots for these nanocubes are
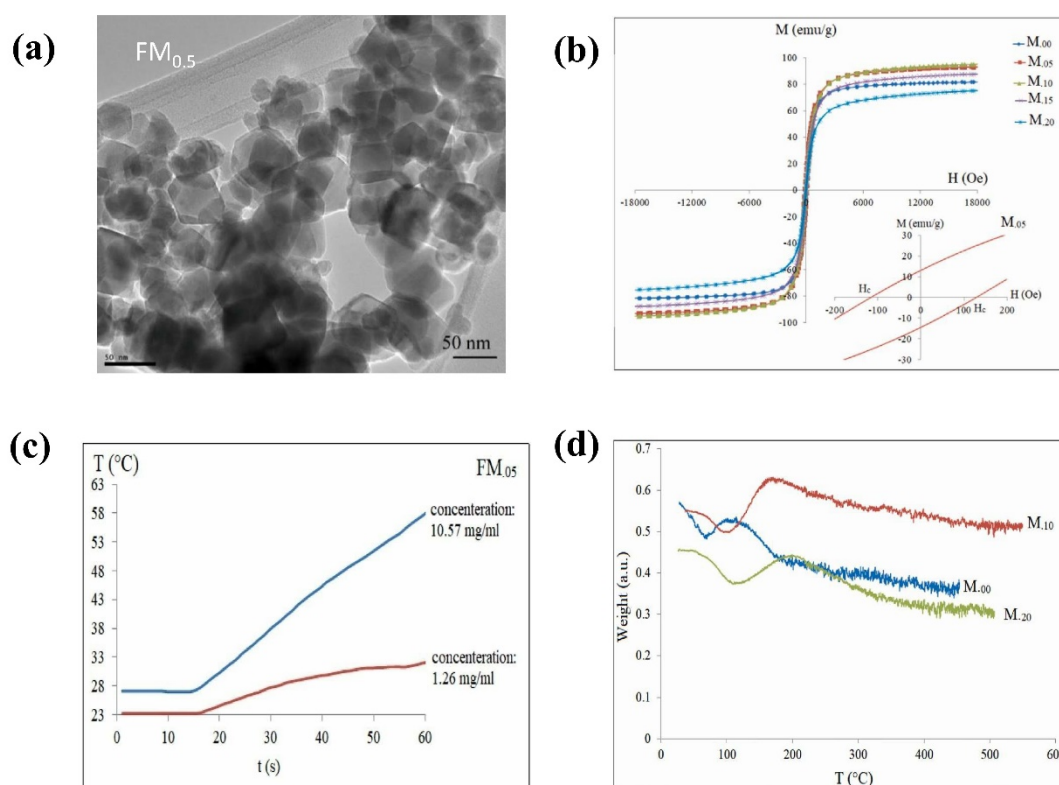
Figure 7. (a) TEM image of the cubical ZFNPs produced using a co-precipitation method. (b) The plot of magnetization with respect to the changing magnetic field for cubic ZFNPs of varying composition. (c) The temperature time dependence of the ZFNP-based ferrofluid at concentrations of 1.26 mg/mL and 10.57 mg/mL. (d) The TG response of cubical ZFNPs showing excellent thermal stability. (Reproduced with permission from ref.[45]. Copyright 2022, ELSEVIER).

ARTICLE

shown in **Figure 8. (b).** Zinc substitution in ferrites have observed very high saturation magnetization values, in the range of ~ 130 emu/g_{Fe+Zn}. The rise in temperature with time of of different Zn and Co doped ferrite-based ferrofluids in the presence of alternating magnetic field were recorded (**Figure 8. (c)**). Herein, zinc doped ferrites clearly show better heating capability when compared with the cobalt doped ferrite particles. The SAR values for these nanocubes obtained under an applied magnetic field of 23 kA/m and a frequency of 293 kHz were dependent on both the zinc doping concentration and the size of the nanocubes produced. The maximum SAR achieved was 1675 W/g for a stoichiometric composition of $Zn_{0.3}Fe_{2.7}O_4$ and a cube dimension of ~ 40 nm. The variation of the SAR with respect to zinc doping concentration is shown in **Figure 8. (d)**. As we can see in this figure, the SAR increases until a zinc doping concentration of x = 0.3 is achieved. These nanocubes have achieved extraordinary SAR and magnetic properties due to the synthesis procedure adopted which produces

highly uniform sized nanoparticles and excellent dispersive ferrofluid. The anisotropic behavior of the ZFNPs is the reason attributed to these excellent hyperthermia properties.

The anisotropy can be further increased by producing particles of unequal dimensions; for example, shapes such as octahedral and faceted polyhedral are a few of the morphologies that can provide more significant changes in the anisotropic behavior. However, research on these types of particles is limited. One of the recent studies in this area was conducted by Rubio *et al*.[71], who proposed a thermal decomposition method of metal oleates to tune the morphology as well as the size of the nanoparticles. Their method is capable of producing spherical, cubical, octahedral and faceted polyhedral shapes, along with fine conrol of the size and dispersion of these nanoparticles The TEM images of the various polyhedral shaped particles produced is shown in **Figure 9. (a)**.
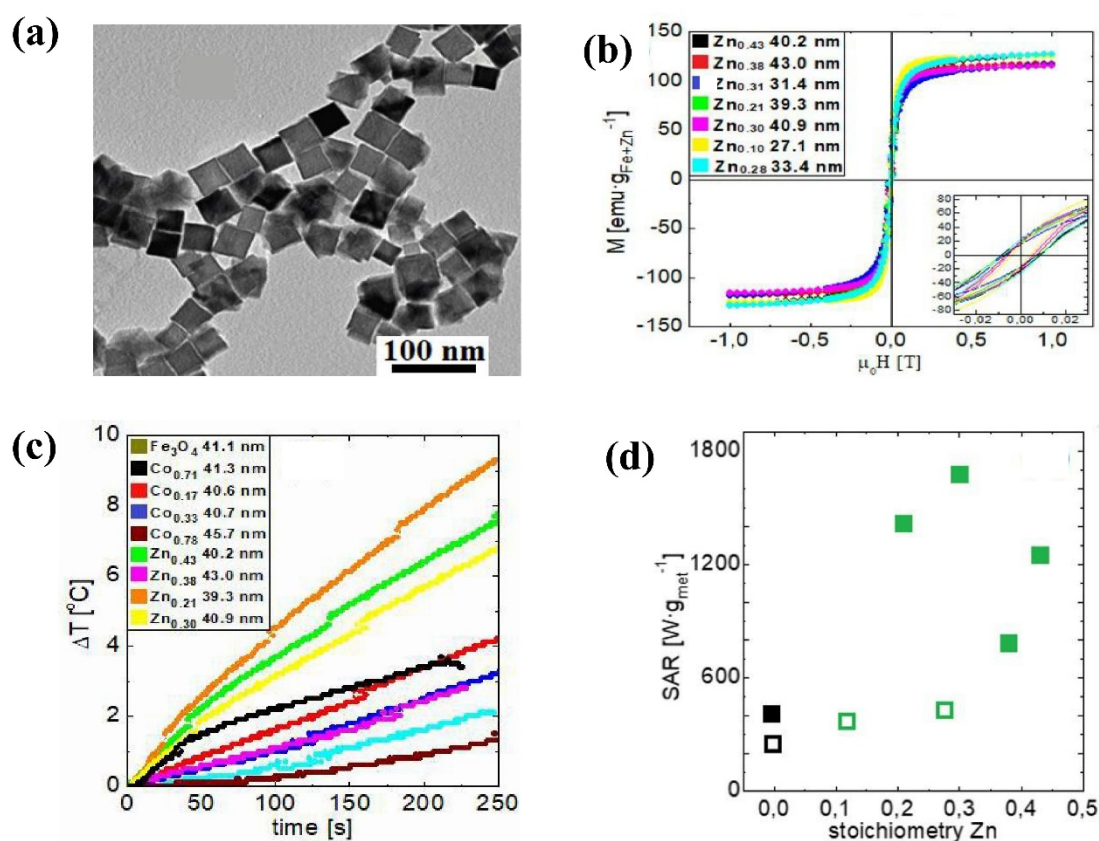
Figure 8. (a) TEM image of the ZFNPs prepared using thermal decomposition method. b) The magnetization response of ZFNPs in varying magnetic field. (c) The relative change in temperature obtained with respect to time in the presence of alternating magnetic field. (d) The variation of SAR with respect to Zn composition. (Reproduced with permission from ref.[89]. Copyright 2021, American Chemical Society).

ARTICLE
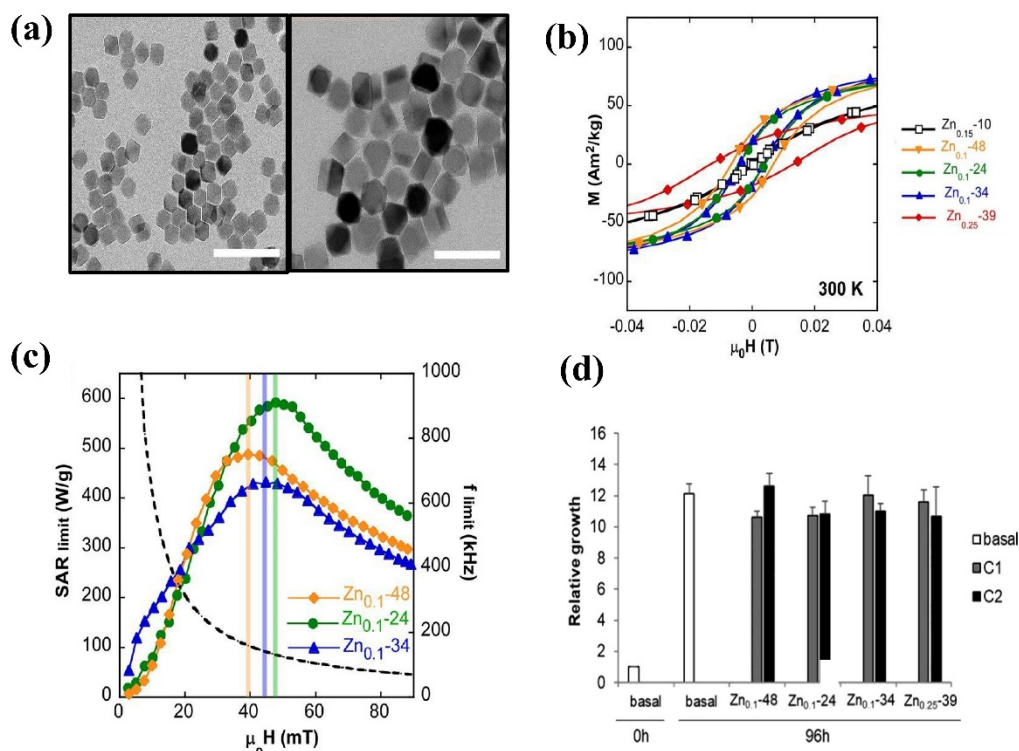
Figure 9. (a) TEM images of the octahedral (left) and faceted polyhedral (Right) NPs produced by chemical decomposition of metal oleates. The scale bars in white are equivalent to 100 nm. (b) Magnetization curves at 300K for the various Zn doped ferrite polyhderas. (c) The SAR variation of the various compositions of ZFNP at varying magnetic field intensity and frequency. (d) The cell viability test results after the incubation of human colorectal cancer cells with ZFNPs for 96 hrs (Reproduced with permission from ref.[71]. Copyright 2021, American Chemical Society).

dependent magnetization studies show a small change in saturation magnetization. The room temperature M_s was recorded to be 97 emu/g, which was reduced to 90 emu/g for the highest doped sample. The room temperature magnetization curve is shown in **Figure 9. (b).** The hyperthermia properties of these samples, recorded by applying an additional coating of PMAO-PEG (PMAO-dodecylamine-modified poly- (isobutylene-alt-maleic anhydride) polymer, PEG-polyethylene glycol), were conducted under magnetic fields of 70.02, 51.72, 42.17 kA/m at frequencies of 153, 300, 605 kHz, respectively. The SAR values achieved were high (> 1000 W/g), with the maximum achieved being 3652 W/g for the smallest sample having an average dimension of 24 nm at a field strength of 53 mT and a frequency of 605 kHz. These results were interpolated using the Hergt Criterion for frequency cutoff, [90] and the maximum SAR or SAR limit was calculated for various samples. The plot of the SAR limit variation under magnetic field and frequency is shown in **Figure 9. (c).** The human colorectal cancer cells were incubated with the

nanoparticle solution for 96 hrs, and their growth relative to their size at incubation is considered as the cell viability performance. The near basal growth in almost all the incubated samples shows that the cytotoxity is minimal for these nanoparticles (**Figure 9. (d)**).

The polyhedral ZFNPs show good promise in terms of hyperthermia and magnetic properties. However, they have been the subject of limited resarch. Additonal recent work in this context has been reported by Yang *et al*. [91], Starsich *et al*. [92], and He *et al*. [93] It is unexpected that superparamagnetic ZFNPs of cubic and octahedral morphologies are not reported in the current literature available; however, the reason for this limited research may be because it is one domain that needs to be more thoroughly explored to fabricate shape modified pure zinc ferrite nanostrcutures for enhanced hyperthermia performance. A summary of the research published using pure ZFNPs is listed in **Table 3**. Better performance perhaps is achieved through the doping of other transition metals.

Table 3. Zinc Ferrite Nanoparticles and their critical properties for Hyperthermia applications

Material	Coating or Modification	Morphology	Particle Size (nm)	M_s (emu/gm)	SAR (W/gm)	H (kA/m)	f (kHz)	T_{Max} (^{0}C)	t_{exp} (min)	t_{42} (min)	Ref
$Zn_{0.52}Fe_{2.48}O_4$	C-Chistosan (+)	Spherical Clusters	8-10	87	264	27-35	360	46	12	5	[33]
$Zn_{0.1}Fe_{2.9}O_4$	--	Spherical	12.4	82	139	7.5	339	--	10	--	[34]
$ZnFe_2O_4$	Oleic Acid	Spherical	23.63	23.59	105	35	350	46	20	5	[36]
$Zn_{0.37}Fe_{2.63}O_4$	Citric acid	Spherical	10.3	90.23	106.4	15.9	252	36	1.67	--	[44]
$Zn_{0.37}Fe_{2.63}O_4$	Citric acid	Spherical	10.3	90.23	261.2	15.9	577	44	1.67	1.33	[44]
$Zn_{0.3}Fe_{2.7}O_4$	Citric Acid (CA)	Spherical	10.42	79.89	28.1	6	330	--	--	--	[50]
$Zn_{0.37}Fe_{2.63}O_4$	Citric Acid (CA)	Spherical	9.8	82.5	18.03	6	330	--	--	--	[50]
$ZnFe_2O_4$	Oleic Acid	-	12.30	25.87	-	4	265	47	20	10	[22]
$Zn_{0.4}Fe_{2.6}O_4$	DMSA	Spherical	15	152	-	-	-	-	-	-	[51]
$Zn_{0.63}Fe_{2.37}O_4$	dDPMA	Spherical	8.2	78	17.5	-	-	-	-	-	[52]
$ZnFe_2O_4$	Gongronema Latifolium	Spherical Clusters	20-40	0.012	142.6	11.54	425	45.05	5	3	[53]
$Zn_{0.2}Fe_{2.8}O_4$	Citric Acid	Spherical Clusters	14.3	0.504	225	15.91	87	-	-	-	[54]
$ZnFe_2O_4$	Allium Cepa	Spherical	23-55	61.32	32.60	14.32	425	46	5	4	[55]
$ZnFe_2O_4$	ZDS	Spherical Clusters	17	36.5	393	35.33	316	50	4	2	[88]
$Zn_{0.1}Fe_{2.9}O_4$	Citric Acid + Pluronic F-127	Cubic	26	95.2	373	16	290	58	1	0.5	[45]

$Zn_{0.05}Fe_{2.95}O_4$	Citric Acid + Pluronic F-127	Cubic	28	93.2	539	16	290	-	-	-	[45]
$Zn_{0.29}Fe_{2.710}O_4$	P-mPEG	Octahedral	-	106.8	-	-	240	-	-	-	[91]
$Zn_{0.468}Fe_{2.532}O_4$	Oleic Acid	Faceted Polyhedral	-	109.7	-	-	240	-	-	-	
$Zn_{0.522}Fe_{2.478}O_4$		Cubic	-	104.4	-	-	240	-	-	-	
$Zn_{0.3}Fe_{2.7}O_4$	SiO$_2$	Cubo-Octahedron	18-22	0.458	1010	13	380	54	3	2	[93]
$ZnFe_2O_4$	Tetra methyl ammonium Hydroxide	Polyhedral (pH=9)	15.43		45	5-65	355	39	5	-	[63]
			12.2								
$ZnFe_2O_4$	Tetra methyl ammonium Hydroxide	Spherical (pH= 12)	24.97	11	125	5-65	355	49	5	2	[63]
$Zn_{0.9}Fe_{2.1}O_4$	Tetra-ethylene glycol (TEG)	Spherical	11	12	36	2.7	700	38.6	6	-	[94]
$Zn_{0.13}Fe_{2.87}O_4$	Oleic Acid Oleylamine	Cubo-Octahedron	18.3	86.2	525	23.87	228	290	480	0.5	[21]
$ZnFe_2O_4$	Diethylene Glycol (DEG)	Quasi-Spherical	8.5	41.06	42.26	26.68	276	48	20	6	[95]
$Zn_{0.3}Fe_{2.7}O_4$	Citric Acid	Cubic	13- 25	35.86	18.706	6	330	51	25	11	[80]
$ZnFe_2O_4$	Oleic Acid Olelyamine	Spherical	10	38.9	128.76	9.95	315	50	12	7	[96]

5. Mn-Zn ferrite nanostructures for MHT applications

Recent research has turned to examining the properties of doped zinc ferrite-based nanosystems, with a number of studies focusing on the incorporation of manganese into zinc ferrite nanostructures because of their potential applications in cancer theranostics. The Mn-Zn ferrite nanostructures including Mn and Zn codoped magnetite nanosystems have exhibited excellent biocompatibility, potentially exceptional magnetic properties and more importantly, an outstanding magnetic hyperthermia performance for practical applications.[97–103] In this section, we primarily discuss the morphological aspects, magnetic properties and hyperthermic potential, including *in vivo* studies based on mice-models, of Mn-Zn ferrite-based nanostructures. These nanomaterials exhibiting different morphologies that can be synthesized using the various techniques depicted in **Figure 10**.[104] Over the last few years, a number of pre-clinical studies based on zinc ferrite systems

ChemComm
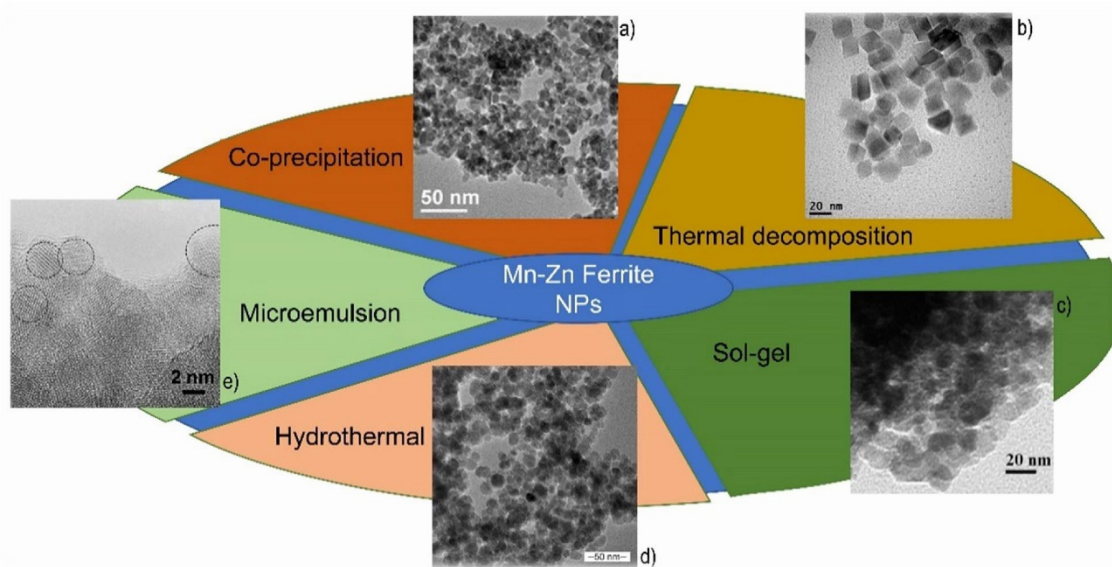
ARTICLE

Figure 10. Schematic representation of the different morphological Mn-Zn ferrite nanoparticles synthesized using (a) Co-precipitation, (b) Thermal decomposition, (c) Sol-gel, (d) Hydrothermal and (e) Microemulsion for biomedical applications. (Reproduced with permission from ref.[104]. Copyright 2021, MDPI).

have been conducted using functionalized Mn-Zn ferrite nanostructures.

First, we analyze a system comprised of manganese and zinc co-doped magnetite nanoparticles recently investigated by L.B. de Mello *et al*.[97], who synthesized these co-doped PEGylated nanoparticles that exhibit the truncated octahedron morphologies seen in **Figure 11. (a-b)** via a simple co-precipitation approach. Several nanoparticle samples of $Zn_xMn_yFe_{1-(x+y)}Fe_2O_4$ with stoichiometry were fabricated by systematically varying the concentration of manganese and zinc. Furthermore, the corresponding saturation magnetization (M_S) as well as the magnetic hyperthermic potential of these co-doped samples was investigated, with the results finding that the nanoparticles display nearly superparamagnetic behavior, i.e., zero coercivity and remanence, and that the highest saturation magnetization was reported to be ~81 emu/g at room temperature (300 K) for an equimolar concentration of zinc and manganese co-doping **(Figure 11. c)**. However, the SAR was reported to be much lower at ~ 25 W/g compared to ~ 38 W/g and 46 W/g for $(Zn_{0.1}Mn_{0.3}Fe_{0.6})Fe_2O_4$ (M_S ~ 74 emu/g) and $(Mn_{0.4}Fe_{0.6})Fe_2O_4$ (M_S ~ 72 emu/g) nanoparticle samples, respectively. The increase in temperature, reported as ΔT *vs.* time plots for all the nanoparticle samples including a control,

namely citric acid solution, can be seen in Figure **11. (d)**. The higher concentration of zinc leads to a reduction in the saturation magnetization as the presence of paramagnetic zinc may possibly affect the super-exchange interactions between the metal-oxygen ions in the spinel structure. The presence of zinc further reduces the SAR values, with the lowest magnitude of ~ 4 W/g recorded for $(Zn_{0.4}Fe_{0.6})Fe_2O_4$ nano systems. As seen in **Figure 11. (d)**, the increase in temperature during the first 10 min, or 600 sec, of magnetic hyperthermia is the highest for $(Mn_{0.4}Fe_{0.6})Fe_2O_4$ followed by $(Zn_{0.3}Mn_{0.1}Fe_{0.6})Fe_2O_4$. Therefore, it is critical to determine the optimal concentration of zinc and manganese needed in the ferrite spinel configuration to obtain enhanced SAR values and, correspondingly, the appropriate heating impact during magnetic hyperthermia. The incorporation of manganese plays a crucial role in modifying the magnetic properties as well as the SAR of spinel ferrite nanoparticles. It is of particular interest that the inclusion of manganese in zinc ferrite nano systems can register a magnetic saturation as high as ~ 175 emu/g as was observed for $(Zn_{0.4}Mn_{0.6})Fe_2O_4$ synthesized by a typical one-pot thermal decomposition method.[105] In addition to Mn doping, it has been observed that surfactants like oleic acid or polyethylene glycol (PEG) strongly influence the shape anisotropy, magnetic properties, and self-heating abilities for magnetic hyperthermia applications of Mn-Zn ferrite-based nanomaterials.[100]

ARTICLE
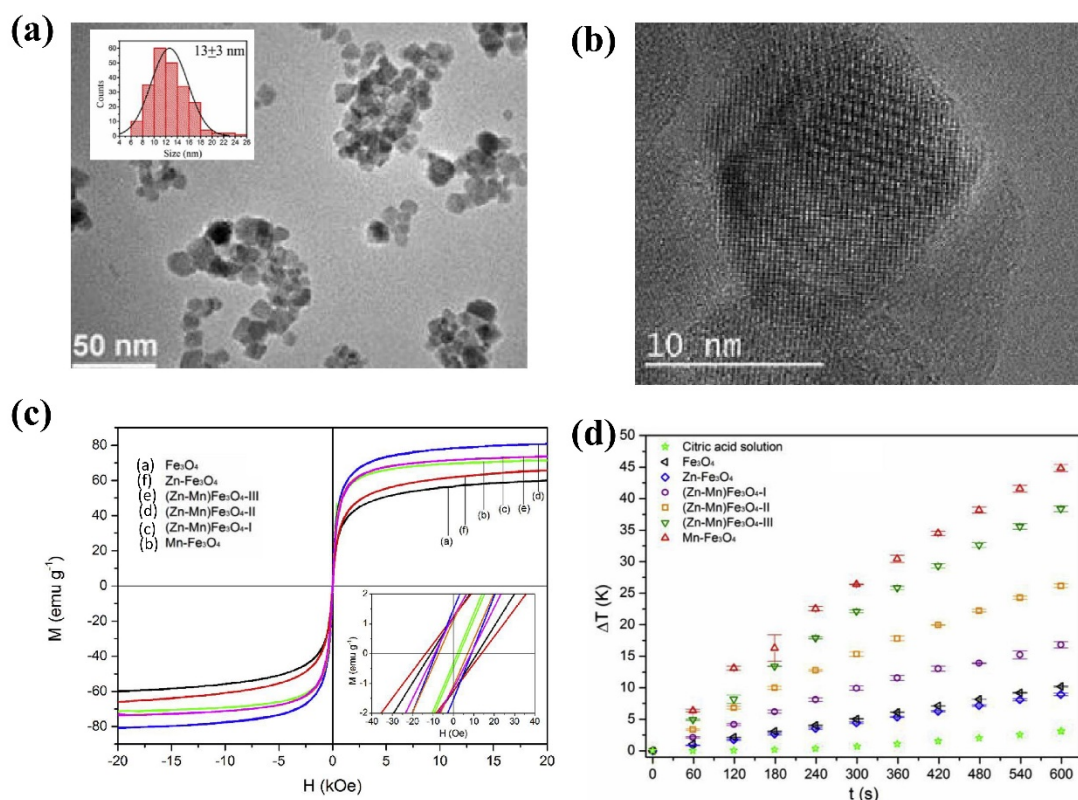
Figure 11. (a) TEM (b) and high resolution TEM image of PEG coated $(Mn_{0.1}Zn_{0.3}Fe_{0.6})Fe_2O_4$ magnetic nanoparticles having truncated octahedral morphology and average particle size of 13 ± 3 nm, (c) field dependent magnetic hysteresis plot, and (d) hyperthermia plot over 600 s. (Reproduced with permission from ref.[97]. Copyright 2019, ELSEVIER).

In a recent study, Lin Wang *et al.*[98] reported the fabrication of water-soluble amphiphilic vitamin E (d-alpha-tocopheryl polyethylene glycol 1000 succinate) functionalized Mn-Zn ferrite nanoparticles, denoted MZF@TPGS, as a potential candidate in cancer theranostics. Doped zinc ferrite nanostructures of varying Mn concentrations were synthesized using a thermal decomposition method, the TEM image of one such Mn-Zn ferrite nano system, $Mn_{0.5}Zn_{0.5}Fe_2O_4$ (MZF), shown in **Figure 12. (a)**, exhibiting uniformly distributed spherical morphology of dimensions 10.35 ± 1.25 nm. The inset of **Figure 12. (a)** shows the TEM image of MZF@TPGS nanoparticles with a size distribution of 153.39 ± 17.52 nm. Most importantly, the magnetic saturation of $Mn_{0.5}Zn_{0.5}Fe_2O_4$ was the highest at ~ 82 emu/g at 300 K. This result is interesting because for the system comprised of Mn and Zn co-doped magnetite[97] mentioned earlier, the highest M_S was recorded for an equimolar co-doping of manganese and zinc. In this case, the sample containing equimolar amounts of manganese and zinc, $Mn_{0.5}Zn_{0.5}Fe_2O_4$ was subjected to TPGS functionalization. The saturation

magnetization of the MZF@TPGS formulation was recorded to be ~ 45 emu/g (**Figure 12. (b)**). However, the coercivity is found to be reduced to 0.184 kA/m compared to 0.263 kA/m for MZF. Furthermore, the cytotoxicity studies conducted on the KB model of cancer cells incubated with the MZF@TPGS formulation for 24 h showed no significant toxicity effects up to a concentration of 20 μg Fe/ml (**Figure 12. (c)**). However, after the post-hyperthermia (H=10 Oe, *f* = 100 kHz, t= 30 min) treatment (MZF@TPGS+hyperthermia+24h incubation), a drastic decrease in the cell viability is observed at a concentration of 20 μg Fe/ml. In addition, these researchers investigated the *in vivo* hyperthermia (H = 20 Oe, *f* = 100 kHz, t = 30 min) potential of the MZF@TPGS formulation on KB tumor cell-bearing mice, reporting a significant reduction in tumor volume after 17 days for the group of mice treated with MZF@TPGS + hyperthermia compared to the control treated with PBS and no hyperthermia for the MZF@TPGS conditions (**Figure 12. (d)**). Of particular importance is the fact that this significant inhibition in the tumor volume was achieved after

ARTICLE
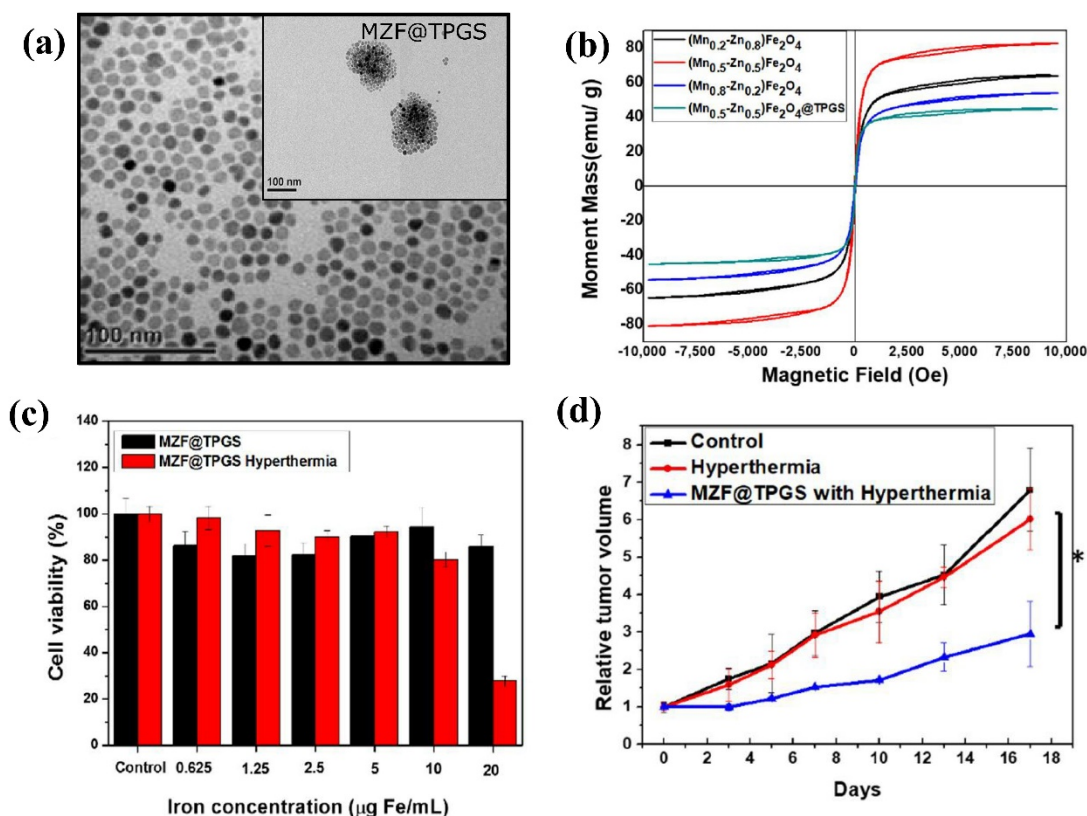
Figure 12. (a) TEM image of $Mn_{0.5}Zn_{0.5}Fe_2O_4$ (MZF) magnetic nanoparticles having a spherical morphology and average particle sizes of 10.35 ± 1.25 nm with inserted TEM image of d-tocopheryl polyethylene glycol 1000 succinate MZF (MZF@TPGS) with an average particle size of 153.39 ± 17.52 nm. (b) The hysteresis loops of various Mn/Zn ratio MZF nanoparticles (black: $Mn_{0.2}Zn_{0.8}Fe_2O_4$, red: $Mn_{0.5}Zn_{0.5}Fe_2O_4$, blue: $Mn_{0.8}Zn_{0.2}Fe_2O_4$, green: $Mn_{0.5}Zn_{0.5}Fe_2O_4$@TPGS) and TPGS formulated $Mn_{0.5}Zn_{0.5}Fe_2O_4$ nanoparticles formulations (MZF@TPGS). (c) Cell viability of KB cells under the treatment of MZF@TPGS, (d) *In vivo* antitumor effect studies of MZF@TPGS formulations in KB tumor-bearing mice, decrease in tumor size. (Reproduced with permission from ref.[98]. Copyright 2022, *Pharmaceutics*).

only a single hyperthermia treatment, meaning MZF@TPGS played a vital role in delivering an impactful tumor regression effect at a relatively low and safe field-frequency. Over the last few years, it has been observed that magnetic hyperthermia can be productive when applied in conjunction with other traditional treatment modalities. In a recent study conducted by Wang *et al.* [101], the researchers exploited Mn-Zn ferrite nanomaterials to deliver a synergistic therapy for lung cancer treatment involving a combination of magnetic hyperthermia and radiotherapy. In this work, Mn-Zn ferrite or MZF ($Mn_{0.6}Zn_{0.4}Fe_2O_4$) spherical nanoparticles were synthesized using a thermal decomposition technique. Then, using a self-assembly approach, these MZF nanoparticles were encapsulated in micelles (NH_2-PEG_{2000}-PCL_{3400}), which render

their surfaces amino-functionalized. Finally, the hyaluronic acid modified MZF nano systems, denoted by MZF-HA (diameter ~ 150 nm), were fabricated using EDC/NHS chemistry (**Figure 13. (a)**). The TEM image of $Mn_{0.6}Zn_{0.4}Fe_2O_4$ (MZF) nanoparticles, along with inserted TEM image of MZF-HA is shown in **Figure 13 (b)**. The magnetic hysteresis curves of both MZF and MZF-HA are shown in **Figure 13. (c)**. The MZF nanoparticles exhibit a saturation magnetization as high as ~ 55 emu/g compared to 6.8 emu/g for MZF-HA. However, both MZF and MZF-HA have near zero residual magnetization confirming their superparamagnetic behavior. **Figure 13. (d)** shows the change in temperature *vs* time plots of MZF-HA under alternating magnetic fields (f=178 kHz; I= 64.1 A). The temperature reaches the optimum target ~ 43 °C within 7 min at a concentration of 2

mg of Fe/ml. In clinical applications, a control heat treatment is a necessity; hence, fixing the self-heating temperature at ~ 43 °C is crucial. Despite having a low value of saturation magnetization, the effective SAR reported for MZF-HA is significantly higher, 247.2 W/g at a concentration of 2 mg of

Fe/ml. The hyaluronic acid functionalization facilitates the uptake of these Mn-Zn ferrite nanoparticles into the human lung adenocarcinoma cell line, the A549 cells, via the binding of CD44, a cell surface adhesion receptor overexpressed on the surface of these cancer cells.
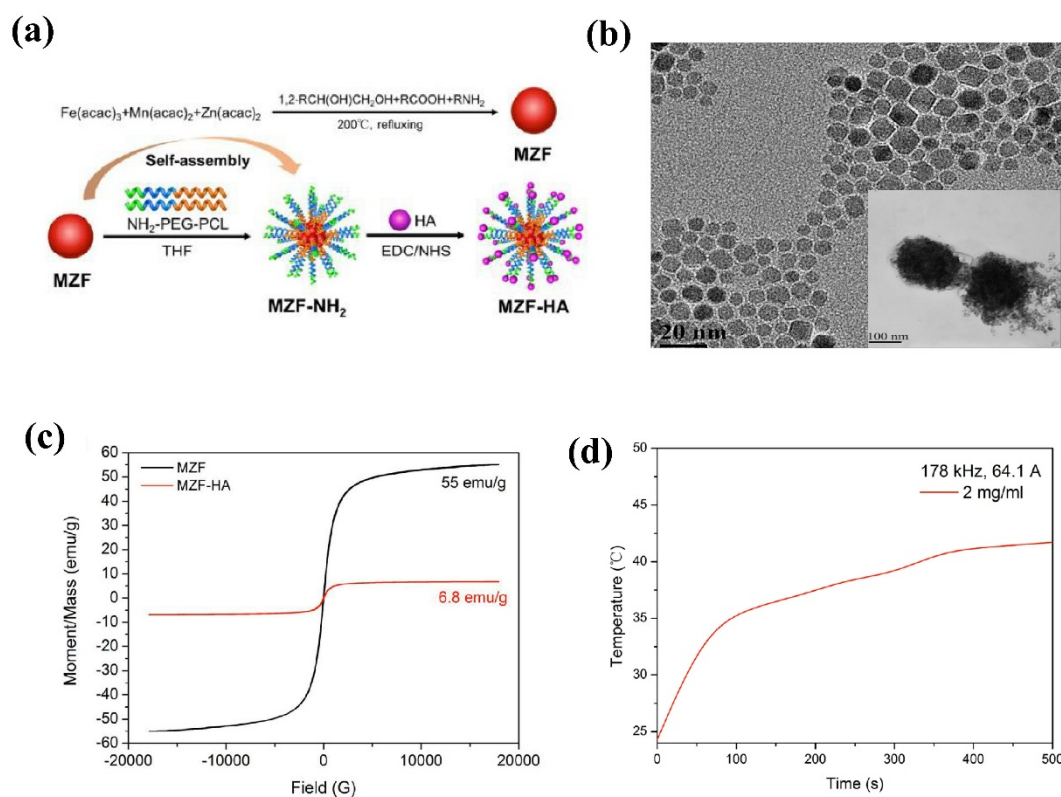
Figure 13. (a) Schematic representation of the synthesis process of $Mn_{0.6}Zn_{0.4}Fe_2O_4$(MZF) and its post modification with hyaluronic acid. (b) TEM image of $Mn_{0.6}Zn_{0.4}Fe_2O_4$ (MZF) nanoparticles, with inserted TEM image of MZF-HA). (c) Magnetic hysteresis loop of MZF nanoparticle and MZF-HA. (d) Temperature profile curve of hyaluronic acid modified $Mn_{0.6}Zn_{0.4}Fe_2O_4$ (MZF-HA) at an external induction field of 178 kHz and 64.1 A (Reproduced with permission from ref.[101]. Copyright 2020, American Chemical Society).

For the *in vivo* anticancer treatment, four groups of mice were labelled as (i) control where PBS is injected to mice; (ii) hyperthermia (HT) containing MZF-HA in presence of alternating magnetic field (AMF); (iii) Radiotherapy (RT) (only RT treatment); and (iv) combined group of hyperthermia and radiotherapy (MZF-HA + AMF + RT). The HT was applied after RT for 30 min at 178 kHz using a current of 64.1 A. The researchers performed the treatment on a tumor volume of 80 mm³. The effect of different treatment condition based on relative change in tumor volume is depicted in **Figure 14. (a)** and **(b)**. The effect of the four treatment conditions was analyzed for a total of four hyperthermia cycles on Day 1, Day 4, Day 7 and Day 13. For treatment condition of RT and RT + HT, the mice were subjected to 12 Gy irradiation in each fraction on a day. The tumor volume decreased to 49 % under the combined treatment of hyperthermia and radiotherapy in Day 13 (**Figure 14. (b)**).

However, the tumor volume increased to 58.8 % in the control group.

In a recent study conducted by Wang *et al*.[106], a sophisticated platform based on the anti-cancer drug doxorubicin and functionalized Mn-Zn ferrite nanoparticles embedded in an injectable hydrogel, specifically PULL-CS hydrogel, was explored as a synergistic magnetothermal-chemo-chemodynamic therapy. In addition to demonstrating magnetic hyperthermia and chemotherapy potential, this nanocomposite hydrogel system actively participates in catalysis producing *in-situ* hydroxyl radicals via Fenton-like reactions, further facilitating in cancer cell annihilation. The Mn-Zn ferrite nanospheres, $Mn_{0.6}Zn_{0.4}Fe_2O_4$, synthesized using a thermal decomposition technique and having a similar stoichiometry to the previously mentioned Mn-Zn ferrite system [101], were functionalized with mesoporous silica and the fluorescent dye Rhodamine B isothiocyanate (RBITC), denoted by MMSN-RBITC,

ARTICLE
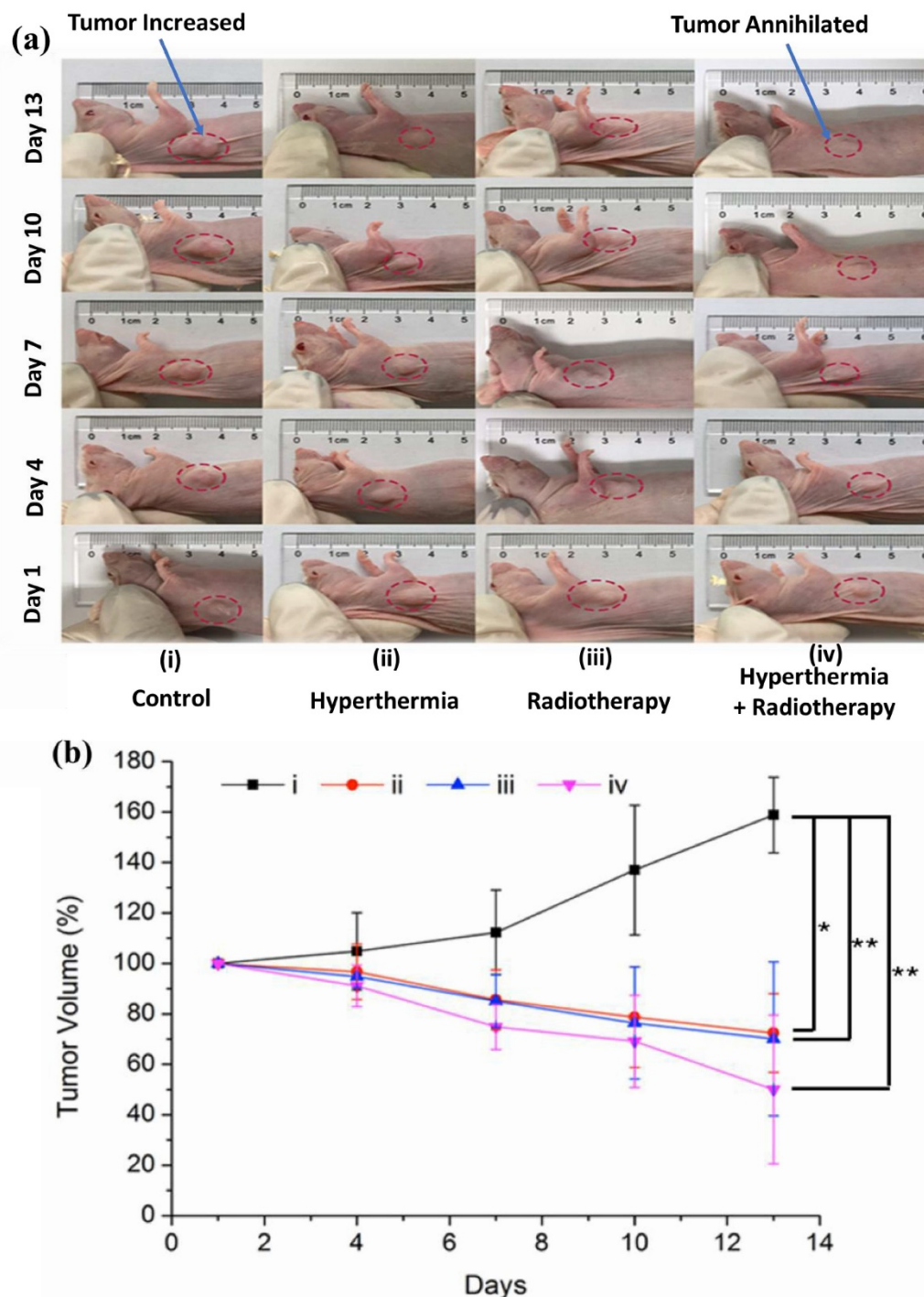
Figure 14. (a) Schematic representation of tumor size in mice. (b) Plot of rate of tumor volume change for different treatment groups (i) control group, PBS injection via tail vein; (ii) HT group, treated with MZF-HA and AMF; (iii) RT group, treated with RT only; and (iv) hyperthermia plus radiotherapy group, treated with MZF-HA and AFM plus RT, where treatment was performed on Days 1 and 4. (Reproduced with permission from ref.[101]. Copyright 2020, American Chemical Society).

ARTICLE

using the protocol shown in **Figure 15. (a)**.[106] The TEM images of $Mn_{0.6}Zn_{0.4}Fe_2O_4$ and MMSN-RBITC can be seen in Figure **15 (b)** and **(c)**, with the nanoparticles of the former having an average diameter of ~ 7 nm while the diameter is significantly larger for the MMSN-RBITC nanoparticles. The best size estimate of MMSN-RBITC as determined by dynamic light scattering (DLS) measurements is 30.5 nm. Furthermore, the Mn-Zn ferrite nanoparticles exhibit a saturation magnetization of ~ 64 emu/g which decreases to ~ 52 emu/g, post-functionalization with MMSN-RBITC (**Figure 15. (d)**). The change in temperature *vs* time plots for understanding the hyperthermic potential of this nanocomposite hydrogel system were created based on different concentrations of MMSN-RBITCs suspended in PULL-CS hydrogel under an alternating magnetic field of 328 Oe and a frequency of 160 kHz for 20 min (**Figure 15 (e)**). The temperature profile data obtained depict that with the blank hydrogel, the temperature remains basically unchanged with the passage of time. However, with increasing concentrations of MMSN-RBITCs, the highest temperature achieved after 20 min of hyperthermia was 35 ℃ at 1% /wt. The maximum SAR component for MMSN-RBITCs in hydrogel was estimated to be approximately 642 W/g.
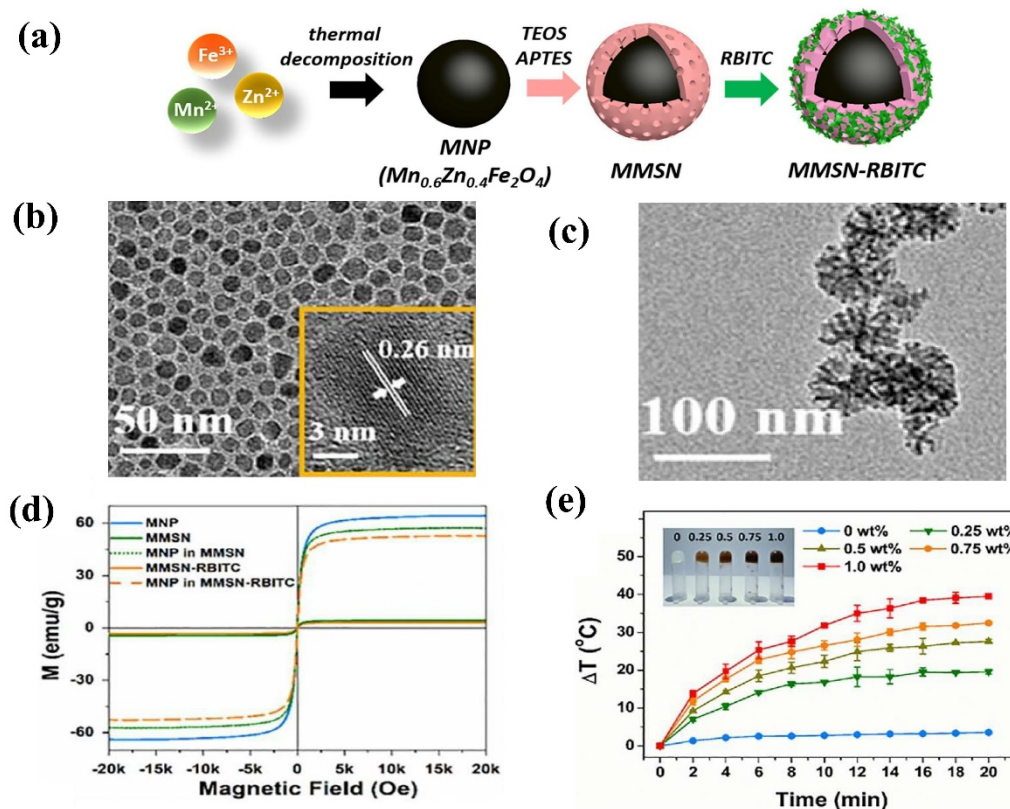
Figure 15. (a) Schematic representation of the synthesis route of MMSN-RBITC. (b) TEM image of $Mn_{0.6}Zn_{0.4}Fe_2O_4$ nanoparticles. (c) TEM image of MMSN-RBITC core shell structure. (d) Hysteresis loop plot of MNP NPs (M_s = 64.09 emu/g), MMSN (M_s = 4.15 emu/g) and MMSN-RBITC (M_s = 3.72 emu/g) nanospheres. (e) Temperature profile curve of nanocomposite hydrogel loaded with different concentrations of MMSN-RBITCs under AMF (160 kHz, 328 Oe). (Reproduced with permission from ref.[106]. Copyright 2020, ELSEVIER).

Furthermore, these researchers investigated the *in vivo* synergistic magnetothermal-chemo and chemodynamic effect on breast tumor (4T1) xenograft mice models. The AMF treated mice groups were subjected to 4 hyperthermia treatment cycles on Day 1, Day 3, Day 5 and Day 7. **Figure 16. (a)** shows the microstructural representation of the PULL-CS hydrogel injected into the mice, and **Figure 16. (b)** depicts the temperature rise (thermal images) in AMF treated mice groups. As these images show, the local temperature of the PBS treated group remains almost unchanged over a period of 7 days. However, for the mice group subjected to injectable hydrogel i.e., Hydrogel + DOX + MMSN-RBITC + AMF, the temperature after 7 days was recorded to be 44.5 ℃, which is within the hyperthermia therapeutic window (**Figure 16. (c)**). In addition as seen in **Figure 16. (d)**, there was approximately an 18-fold increment in the tumor volume after Day 15 for the mice group treated with PBS as opposed to the group injected with the nanocomposite hydrogel and

ARTICLE
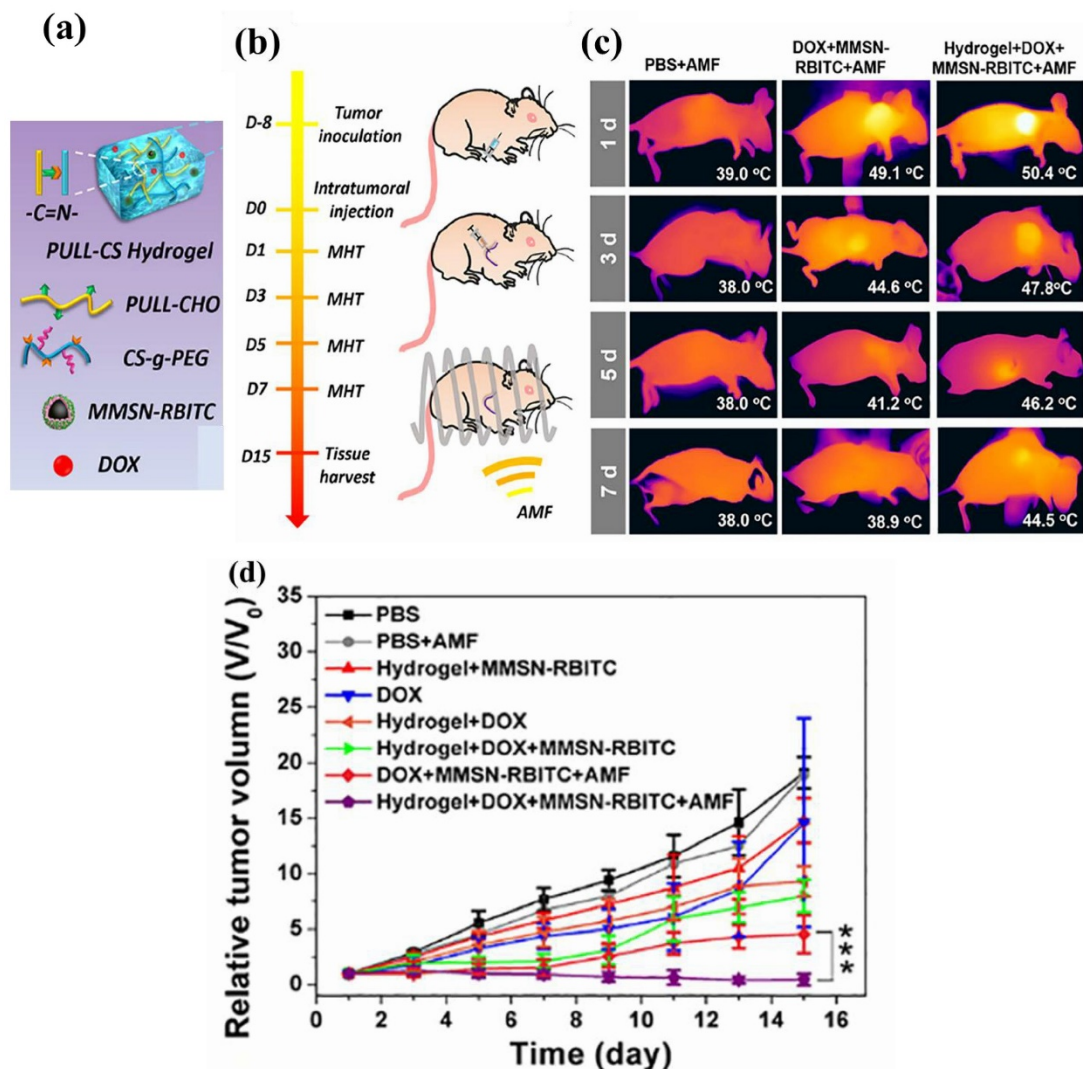
Figure 16. (a) Schematic representation of the microstructure of the PULL-CS hydrogel. (b) Illustration of *in vivo* treatment of 4T1 tumor bearing mice. (c) Picture of the temperature at tumor site after different treatment taken via a near-infrared imager. (d) Plot for relative tumor volume measured at two-day intervals. (Reproduced with permission from ref.[106]. Copyright 2020, ELSEVIER).

subsequently subjected to magnetic hyperthermia treatment (H= 328 Oe, f = 160 kHz, t= 10min). Of particular interest, although the group designated by DOX + MMSN-RBITC + AMF demonstrated substantial tumor regression after 15 days, the most effective anti-

cancer effect is observed with the injectable hydrogel system (Hydrogel + DOX + MMSN-RBITC + AMF). **Table 4** summarizes the magnetic hyperthermia parameters of the Mn- substituted zinc ferrite systems.

Table 4. Mn-Zn ferrite nanostructures and their critical parameters for MHT applications

Material	Coating	Morphology	Particle Size	Ms	SAR (W/gm)	H (KA/m)	f (kHz)	T_{max} (°C)	t_{exp} (min)	t_{42} (min)	Ref

Mn$_{0.06}$Zn$_{0.04}$Fe$_{2.9}$O$_4$	Oleic acid Oleylamine	Cubo-octahedrons	17.2	91.2	426	24	252	-	-	-	[21]
PEG-Mn$_{0.5}$Zn$_{0.5}$Fe$_{6.06}$	PEG	Spherical	17.5	44.4	8.6	14.32	425	74.5	6	1/2	[100]
PEG$_{1.0}$-Mn$_{0.5}$Zn$_{0.5}$Fe$_{5.06}$			19.2	35.5	5.7			48.8		2	
PEG$_{1.5}$-Mn$_{0.5}$Zn$_{0.5}$Fe$_{4.56}$			20.7	30.1	3.5			42.7		5	
Mn$_{0.06}$Zn$_{0.04}$Fe$_2$O$_4$	PEG-b-PCL	Spherical	30	6.8	247	64.1 A	178	43	9	6	[101]
Mn$_{0.2}$Zn$_{0.2}$Fe$_{2.6}$O$_4$	-	Truncated octahedra	8.8	74	16.7	-	-	54	10	5	[102]
Mn-Zn ferrite	*PEG-phospholipids	Spherical-Core shell	15	98	324	12	390	57	15	3	[102]
Zn$_{0.93}$Mn$_{0.03}$Fe$_2$O$_4$	CTAB	Spherical	18.7	91	295	9.2	337	46	23	6	[107]
Mn$_{0.2}$Zn$_{0.2}$Fe$_{2.6}$O$_4$	-	Truncated octahedra	9.7	81	25.1	-	-	43	10	9	[108]
Mn$_{0.6}$Zn$_{0.4}$Fe$_2$O$_4$	mPEG-PCL	Spherical		34.5	1102.4	114.9	114	60	5	2	[109]
Mn0.8Zn0.2Fe2O$_4$				25.9	1037.8	114.9	114	60	5	2	
Mn0.4Zn0.6Fe2O$_4$				25.3	962	114.9	114	60	5	2	
Mn$_{0.2}$Zn$_{0.8}$Fe$_2$O$_4$				21.3	902.2	114.9	114	60	5	2	
Mn$_{0.2}$Zn$_{0.8}$Fe$_2$O$_4$	NIPAAm, HIMAAm	Spherical	-	32.4		6.5	80	56	15	2	[110]

6. Co-Zn ferrite nanostructures for MHT applications

In addition to Mn-Zn ferrite nanosystems, Co-, Ni- and Mg-substituted zinc-ferrite nano-structured materials have also been extensively explored in magnetic hyperthermia studies. First, we will consider Co^{2+} substituted zinc ferrite nanostructures. Co-doped zinc ferrite (Co$_x$Zn$_{1-x}$Fe$_2$O$_4$) shows comparably low Curie temperature (T$_c$); for example, Ibrahim Sharifi et al.[111] investigated superparamagnetic Co$_{0.3}$Zn$_{0.7}$Fe$_2$O$_4$ nano ferrites exhibiting a Curie temperature of ~ 97 °C , with P. Appa Rao et al.[41] reporting a decrease to 46 °C for Co$_{0.37}$Zn$_{0.63}$Fe$_2$O$_4$. It also has excellent magnetic properties, which are beneficial for practical hyperthermia applications.[43,111,112] Continuous efforts have been made by researchers to obtain narrow superparamagnetic Co-Zn ferrites by adopting various fabrication methods.[111,113,114] To address the limitation of the high Curie temperature of Fe$_3$O$_4$ nanoparticles, cobalt-zinc ferrite has seen increased interest. The desired self-controlled heating efficiency can be achieved by tuning the magnetic properties of these nanoparticles.[115] Although obtaining the appropriate hyperthermia temperature range and the large specific absorption rate (SAR) is a challenge at low concentrations, much research has been conducted on Co-Zn ferrite systems aimed at improving their hyperthermia performance. The M$_S$ value of Co-Zn ferrite varies in the range of 40-150 emu/g (shown in **Figure 17. (a-c)**).[116] For example, Andhare et al.[117] investigated the hyperthermia potential of Co$_{0.7}$Zn$_{0.3}$Fe$_2$O$_4$ (CZF) nanoparticles by modifying their surfaces with PEG. The M$_s$ for these PEG-CZF nanoparticles is estimated to be 42.49 emu/g, slightly lower than the uncoated CZF samples (M$_S$ ~ 46 emu/g). The PEG functionalized nanoparticles exhibit better MHT performance, and the hyperthermia temperature (43-45 °C) was reached within 7 to 9 mins. As can be seen in **Figure 17. (d)**, the temperature curves were saturated at 43 °C, 44 °C and 45 °C at nanoparticle concentrations of 4 mg/ml, 6 mg/ml, and 8 mg/ml, respectively. However, at

ARTICLE
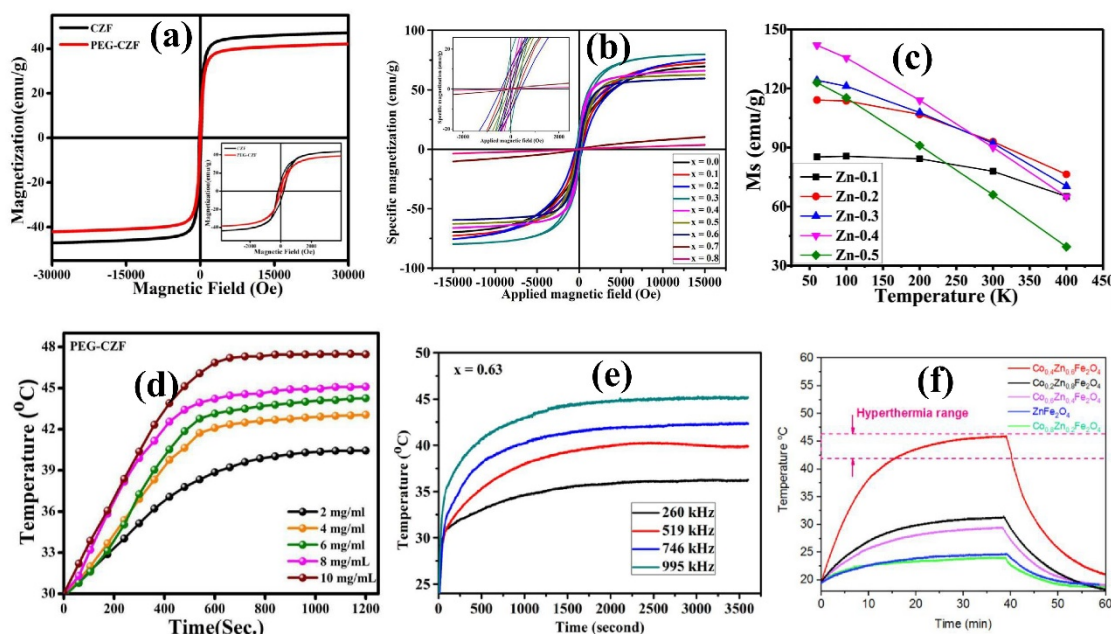
Figure 17. (a) Magnetic hysteresis loop of $Co_{0.7}Zn_{0.3}Fe_2O_4$ (CZF) and PEGylated CZF nanoparticles measured at T = 300 K (Reproduced with permission from ref.[117]. Copyright 2022, Springer). (b) Hysteresis loop of $Co_xZn_{1-x}Fe_2O_4$ (x = 0.0 - 0.8) measured at T = 300 K (Reproduced with permission from ref.[41]. Copyright 2020, ELSEVIER). (c) Variation of saturation magnetization with temperature (T = 60 K 60 K, 100 K, 200 K, 300 K and 400 K) of $Co_{1-x}Zn_xFe_2O_4$ at Zn concentration (x = 0.1, 0.2, 0.3, 0.4, 0.5) (Reproduced with permission from ref.[118]. Copyright 2022, Springer). (d) Induction heating curve of CZF and PEG-CZF for various loaded particle concentrations (Reproduced with permission from ref.[117]. Copyright 2022, Springer). (e) The heating induction curve of $Co_xZn_{1-x}Fe_2O_4$ (x = 0.63) nanoparticles at various applied frequencies (Reproduced with permission from ref.[41]. Copyright 2020, ELSEVIER). (f) Induction heating curve of $Co_xZn_{1-x}Fe_2O_4$ (x = 0.00, 0.2, 0.4, 0.6 and 0.8 with applied frequency (f) = 100 kHz and nanoparticle concentration = 75 mg/ml). (Reproduced with permission from ref.[119]. Copyright 2021, ELSEVIER).

concentrations of 2 and 10 mg/ml, saturation was reached at 40 °C and 47 °C, respectively, one below and one above the threshold temperature of hyperthermia treatment. In addition, the PEG-coated sample produces the highest SAR value of 217.12 W/g for a magnetic nanoparticle concentration of 8 mg/ml.

Furthermore, P. Appa Rao et al.[41] recently reported Co-Zn ferrite $(Co_{0.37}Zn_{0.63}Fe_2O_4)$ nanoparticles, exhibiting a Curie temperature (T_c) as low as 46 °C. Hence, these nanoparticles carry the potency to be the next-generation spinel ferrites, particularly for magnetic hyperthermia applications, as they possess an auto cut-off temperature in the MHT therapeutic window. The magnetization curves of $Co_{1-x}Zn_xFe_2O_4$ (x = 0.0, 0.1, 0.2, 0.3, 0.4, 0.5, 0.6, 0.7 and 0.8) are shown in **Figure 17. (b),** with its highest saturation magnetization being obtained at x = 0.3 (M_s = 79.7 emu/g). The induction heating curve of $Co_{0.37}Zn_{0.63}Fe_2O_4$ is shown in **Figure 17 (e),** and this composition records one of the best hyperthermia performances, reaching the hyperthermia therapeutic temperature (42-46 °C) within ~ 12 mins under an applied field of 15.91 kA/m and a

frequency of 995 kHz at 10 mg/ml particle concentration. Most important, the temperature remains saturated for a period of 30 min and longer, an essential pre-requisite for clinical hyperthermia applications.

Recently, Kumari et al.[118] reported the successful fabrication of cobalt-zinc ferrite fibers $(Co_{1-x}Zn_xFe_2O_4$; x = 0.1, 0.2, 0.3 and 0.4 and 0.5) using an electrospinning method. The plot in **Figure 17 (c)** shows the variation of saturation magnetization at different temperatures for varying Zn concentration in $Co_{1-x}Zn_xFe_2O_4$. The highest room temperature (300 K) saturation magnetization (M_S > 90 emu/g) is obtained at zinc concentrations of x = 0.2, 0.3 and 0.4. These fibers record an excellent MHT performance, which will be explained further in the next section. **Figure 17. (f)** represents the induction heating curve of cobalt zinc ferrite nanoparticles recently reported by Tatarchuk et al.[119]. As this figure shows, the composition of Co-Zn ferrite, $Co_{0.4}Zn_{0.6}Fe_2O_4$, attains the desired hyperthermia temperature within ~ 15 min and remains saturated for a period of 25 min and longer in the MHT therapeutic window.

ARTICLE

Biocompatibility, an important parameter when considering the clinical aspect of magnetic hyperthermia, primarily depends on the type and toxicity of the transition metal ions used in the spinel ferrite nanoparticles and their subsequent release to the cell lines during *in vitro/vivo* applications. The toxic nature of spinel ferrite nanomaterials, given in decreasing order, is $CoFe_2O_4 < Co_{0.5}Mn_{0.5}Fe_2O_4 < Co_{0.5}Cu_{0.5}Fe_2O_4 < Co_{0.5}Zn_{0.5}Fe_2O_4 < Co_{0.5}Ni_{0.5}Fe_2O_4$.[120] Based on this trend, Co-Zn ferrite nanomaterials seem to be a reasonably better biocompatible candidate for cancer theranostics. The following section will further discuss the hyperthermia performance of various Co-Zn ferrite systems.

First we discuss the eradication of cancer cells via superparamagnetic Co-Zn ferrite nanoparticles reported by R. A. Bohara *et al.*[121], who synthesized the cobalt zinc ferrite using a modified thermal decomposition method. The surfaces of the CZF particles were modified with triethylene glycol, the resulting TEM micrographs of the CZF nanoparticles being shown in **Figure 18. (a)**. The particles, characterized by a spherical morphology with an average particle size

of 15 nm, are uniformly distributed. The most frequently reported Co-Zn ferrite nanosystems for hyperthermia applications exhibit a spherical morphology.[41,117,121,122] The room temperature magnetization curve measured at an applied magnetic field of 40 kOe is shown in the inset of **Figure 18. (a)**. As can be seen from the M-H curve, the CZF nanoparticles showed nearly zero coercivity and remanence at zero external field, exhibiting a highly superparamagnetic nature. The saturation magnetization value of these nanoparticles is reported to be 76.53 emu/g. Further, these researchers conducted an induction heating study on Co-Zn ferrite to estimate its hyperthermia performance, the resulting temperature profile curve being shown in **Figure 18. (b)**. This hyperthermia measurement was conducted at AC fields of 167.6, 251.4 and 335.2 Oe for 10 min at particle concentrations of 1, 2, and 5 mg/ml. **Figure 18. (b)** shows the temperature kinetic curve for 2 mg/ml concentration, indicating that the hyperthermia temperature (43 ℃) is reached within 3 min and saturation is attained. The hyperthermia behavior is explained in more detail through the specific absorption rate curve (**Figure. 18 (c)**).
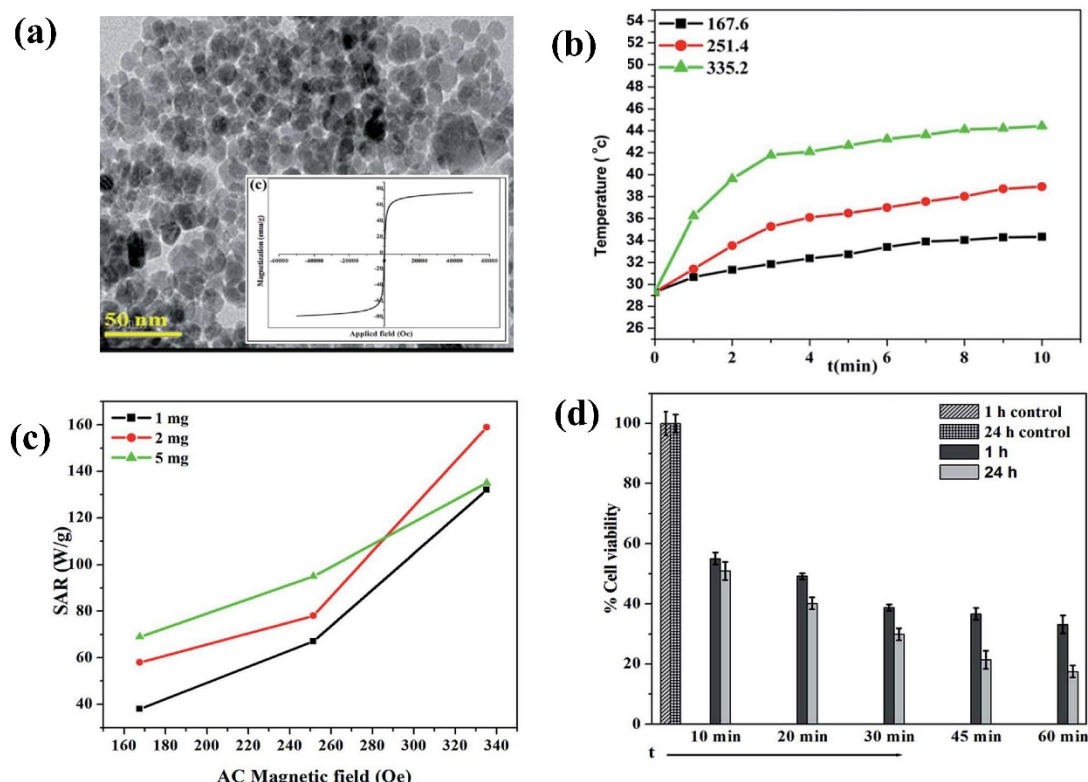
Figure 18. (a) TEM image of cobalt-zinc magnetic nanoparticles showing uniformly distributed spherical morphology, with inserted magnetization curve (M_S = 76.53 emu/g). (b) Induction heating curve with reference to varying AC magnetic fields (167.6, 251.4 and 335.2 Oe) of particle concentration 2 mg/ml. (c) Variation of specific absorption rate with applied AC magnetic field of CZF MNPs. (d) The cell viability study of MCF7 cell lines combined with CZF MNPs for particle concentration of 1 mg/ml for 10 to 60 min at an applied AC magnetic field of 300 Oe and a frequency of 267 kHz incubated for 1 h and 24 h using MTT assay (Reproduced with permission from ref.[121]. Copyright 2015, Royal Society of Chemistry).

ARTICLE

The maximum SAR of 65 W/g is observed at a particle concentration of 2 mg/ml for the applied magnetic field of 335 Oe. The SAR value is almost same for concentrations of 1 and 5 mg/ml at the maximum field of 335.2 Oe. These CZF particles exhibit excellent biocompatibility with different cell assays (MTT- (3-(4,5-dimethyl thiazol-2yl)-2,5-diphenyltetrazolium bromide)) on MCF7 (human breast cancer) and L929 (mouse fibroblast) cell lines. The effectiveness of CZF particles in destroying the MCF7 cells via *in vitro* hyperthermia can be seen in **Figure 18. (d)**. The cell viability after 24 hrs was close to 50 % following a 10 min hyperthermia exposure. However, the percentage decreased significantly to ~ 20 % when the cells were subjected to 60 min of hyperthermia treatment.

One of the most recent and interesting studies on Co-Zn ferrite systems was conducted by Kumari. *et al*.[118], who synthesized Co$_{1-x}$Zn$_x$Fe$_2$O$_4$ (x = 0.1, 0.2, 0.3, 0.4 and 0.5) fibers using an electrospinning method (**Figure 19. (a)**), specifically focusing on using magnetic fibers for magnetic hyperthermia applications. One of the advantages of nano fibers is the small number of canted spins available over the surfaces of fibers, resulting in enhanced magnetic properties in comparison to nano ferrites. The magnetization *vs* applied field curve for Co$_{1-x}$Zn$_x$Fe$_2$O$_4$ (x = 0.4) is shown in **Figure 19. (b)**. These researchers report better magnetization curves for x = 0.4 concentration of zinc in comparison to other concentrations. The magnetization measurement recorded for five temperatures, T = 60 K, 100 K, 200 K, 300 K, and 400 K- as seen in **Figure 19. (b)** show the highest saturation magnetization (M$_s$ ~ 140 emu/g) is obtained at T = 60 K. The room temperature M$_S$ is approximately 100 emu/g.
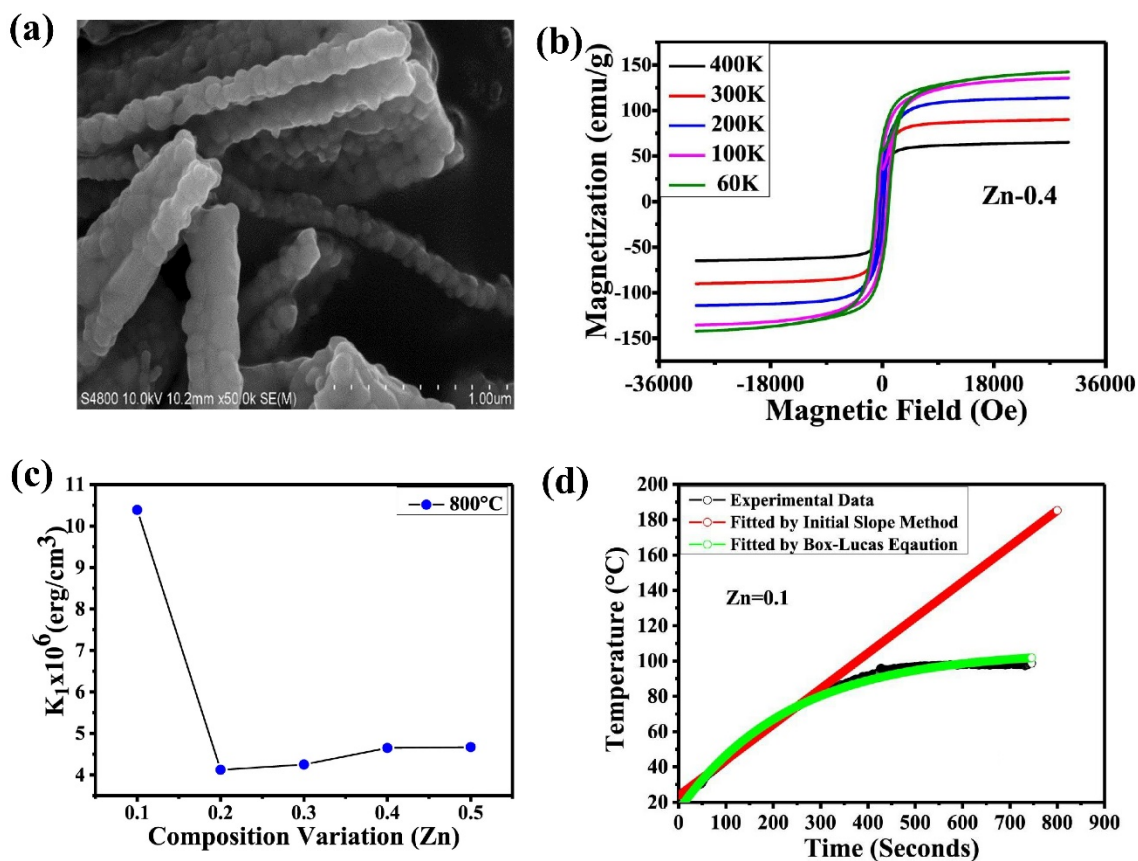
Figure 19. (a) FESEM image of Co$_{0.9}$Zn$_{0.1}$Fe$_2$O$_4$ (CZF) showing fibers morphology. (b) Magnetic hysteresis loop of Co$_{0.6}$Zn$_{0.4}$Fe$_2$O$_4$ at different temperatures (60 K, 100 K, 200 K, 300 K and 400 K) showing saturation magnetization M$_S$ ~ 100 emu/g at 300 K. (c) Curve of effective magnetic anisotropy constant (K$_1$) vs Zn concentration (x = 0.1, 0.2, 0.3, 0.4, 0.5). (d) Magnetic induction hyperthermia plots for Co$_{0.9}$Zn$_{0.1}$Fe$_2$O$_4$. Reproduced with permission from ref.[118]. Copyright 2020, ELSEVIER).

ARTICLE

The variation of magnetic anisotropy constant (K_1) *vs* zinc ion substitution is shown in **Figure 19. (c),** and the induction heating curve is shown in **Figure 19. (d)**. The best hyperthermia result is obtained at x = 0.1 zinc concentration because of the high value of the magnetic anisotropy constant. These nanofibers exhibit high magnetic anisotropy compared to the nanoparticles. As seen in **Figure 19 (d),** the threshold hyperthermia temperature (T = 43 ℃) is reached within ~ 100 s under an applied field and at a frequency of 250 Oe and 336 kHz. The maximum SAR is obtained for $Co_{0.9}Zn_{0.1}Fe_2O_4$ at ~725 W/g. As these results suggest, Co-Zn ferrite

fibers show promise as future nano agents for magnetic hyperthermia applications. **Table 5** summarizes the hyperthermia parameters of co-substituted zinc ferrite nanosystems.

As these discussions and analyses suggest, Co-Zn ferrite nanosystems, based on their superior magnetic properties and excellent biocompatibility, possess significant potential, particularly in delivering a temperature-controlled heating in the MHT therapeutic window (~ 43-46 ℃), which is considered crucial for clinical applications.

Table 5. Co-Zn ferrite nanostructures and their critical parameters for MHT applications

Material	Coating	Morphology	Particle Size (nm)	M_s (emu/g)	SAR (W/g)	H (kA/m)	f (kHz)	T_{Max} (⁰C)	t_{exp} (min)	t_{42} (min)	Ref
$Co_{0.37}Zn_{0.63}Fe_2O_4$	-	Spherical	~ 3.6	~ 59.6	-	15.91	995	46	58	7	[41]
$Co_{0.5}Zn_{0.5}Fe_2O_4$	-	Spherical	19	70.231	114.98	26.67	265	54	15	5	[115]
$Co_{0.7}Zn_{0.3}Fe_2O_4$	-	Spherical	23.94	46.82	166.89	35	280	50	20	4	[117]
$Co_{0.7}Zn_{0.3}Fe_2O_4$	PEG	Spherical	31	42.49	246.09	35	280	47	20	6	[117]
$Co_{0.9}Zn_{0.1}Fe_2O_4$	-	Fiber	35	-	-	19.89	336	-	-	-	[118]
$Co_{0.4}Zn_{0.6}Fe_2O_4$	-	Polyhedral	14	-	2.56	7.95	100	45	60	15	[119]
$CoZnFe_2O_4$	TEG (Triethyl ene glycol)	Spherical	15	76.53	165	26.65	267	45	10	3	[121]
$Co_{0.5}Zn_{0.5}Fe_2O_4$	-	Spherical	12.1	83.7	10	22.9183	-	75	41.66	-	[122]
$Co_{0.2}Zn_{0.8}Fe_2O_4$	-	-	-	85.41	-	19.89	112	95	10	~ 20	[123]
$Co_{0.4}Zn_{0.6}Fe_2O_{4+g}$	Silica	Encapsulated	-	-	-	8.8	484	-	-	-	[124]

7. Ni- and Mg- zinc ferrite nanostructures for MHT applications

The doping of nickel in zinc ferrite nanosystems for hyperthermia applications was first reported in a 2006 study conducted by Lee and Kim,[125] who showed the potential of Ni doped ZFNPs in hyperthermia applications. To understand the hyperthermia-related properties more fully, we first consider the most recent research conducted by P. V. Ramana *et al*.[126], who investigated the hyperthermia

characteristics of citric acid coated and uncoated Ni and Zn co-doped ferrite nanoparticles synthesized using a simple sol-gel method. The TEM image of these Ni doped ZFNPs are shown in **Figure 20. (a)**. The samples showing the appropriate hyperthermia response were those that were annealed at 300 and 400 ℃ since their temperature increases saturated within the hyperthermia therapeutic range. The magnetization response in the presence of an external magnetic field is shown in **Figure 20. (b)**. The NZ3 ($Ni_{0.60}Zn_{0.35}Fe_{2.05}O_4$, annealed at 300 ℃) and NZ4 ($Ni_{0.60}Zn_{0.35}Fe_{2.05}O_4$, annealed at 400 ℃) samples

show a saturation magnetization of 30.8 and 36.3 emu/g, respectively, values similar to those of pure zinc ferrite systems. The hyperthermia studies were conducted in the magnetic field strength of 200 Oe and at the two frequencies of 519 and 746 kHz, using ferrofluids of 12, 14, and 16 mg/ml. To improve the dispersion and the cytotoxicity of these ferrite nanoparticles, a coating of citric acid was applied. The hyperthermia response of these ferro-fluids as a function of time is shown in **Figure 20. (c, d)**; these plots show the hyperthermia response of coated and uncoated NZ3 and NZ4 samples at a frequency of 746 kHz. The uncoated NZ3 samples fail to

reach the therapeutic range; however, the coated particle ferrofluid of the NZ3 samples showed optimum response. The heating curve attains saturation at approximately 45 °C. The t_{42} parameter for this sample was approximately 33 mins, considered a relatively long time. While the NZ4 sample showed the desired response for both the coated and uncoated cases, the performance of the former was better, with a t_{42} parameter of approximately 17 mins, or approximately half the value of the NZ3 sample. However, the heating response was slower compared to the pure zinc ferrite systems found in the literature.
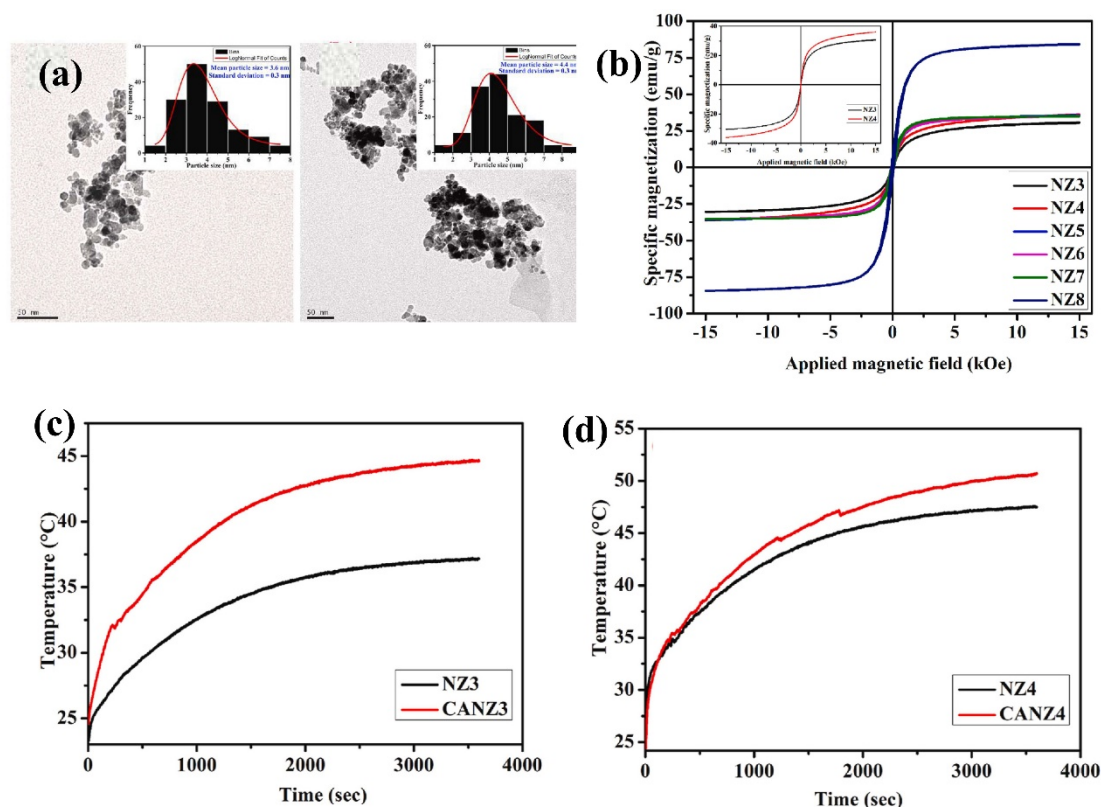
Figure 20. (a) TEM images of the Ni doped ZFNPS annealed at 300^{0}C (NZ3) and 400^{0}C (NZ4) with the inset showing mean particle diameters of 3.6 nm and 4.4 nm. (b) The plot of specific magnetization dependence on the applied magnetic field for various heat-treated Ni doped ZFNPs. (c & d) The plots showing the increase in temperature of the ferrofluid over time for citric acid coated and uncoated NZ3 and NZ4 samples. (Reproduced with permissions from ref.[126]. Copyright 2021, ELSEVIER).

The cytotoxicity, however, shows better performance despite the large concentration of nanoparticles used to prepare the ferrofluid. The Ni doped ZFNPs do not show promising results. A few additional recent studies include those conducted by Kahmei *et al*.[127], Manohar *et al*.[128], Ashfaq Ahmad *et al*.[129], Tovstolytkin *et al*.[130] and Ashfaq Ahmad *et al*.[131] A list of the articles reporting research using Ni doped ZFNPs is given in **Table 6.** These articles found that the saturation magnetization is approximately 30 emu/g for these nanoparticles. However, Kahmei *et al.*[132] reported a saturation magnetization of approximately 60 emu/g.

Most of the reports mentioned have found that the samples with good saturation magnetization do not show heating profiles that

saturate around the hyperthermia therapeutic range, limiting their potential use as hyperthermia agents. Since the remaining hyperthermia related properties are similar to the pure zinc ferrite systems explained previously, researchers have shown less interest in these doped systems. The Ni doped ZFNPs have not shown unique properties like the Mn and Co doped systems. These two factors, the limited number of published articles and no unique property of these zinc ferrite systems, are interrelated. It is possible that the smaller number of studies explains the lack of insight concerning a specific advantage for Ni doping. In addition, it can be concluded that the lack of novelty has led to less exploration of this particular zinc ferrite system and vice versa, meaning there is definitely a need for extensive exploration of the Ni doped zinc ferrite systems. Further,

most of the research reported has synthesized the Ni doped ZFNPs using a sol-gel method, which is a less effective technique for synthesizing uniform sized particles. Other synthesis techniques such as thermal decomposition and auto combustion, among others can

be used to prepare more uniform and better dispersed samples, leading to more improved characteristics than pure zinc ferrite nanomaterials.
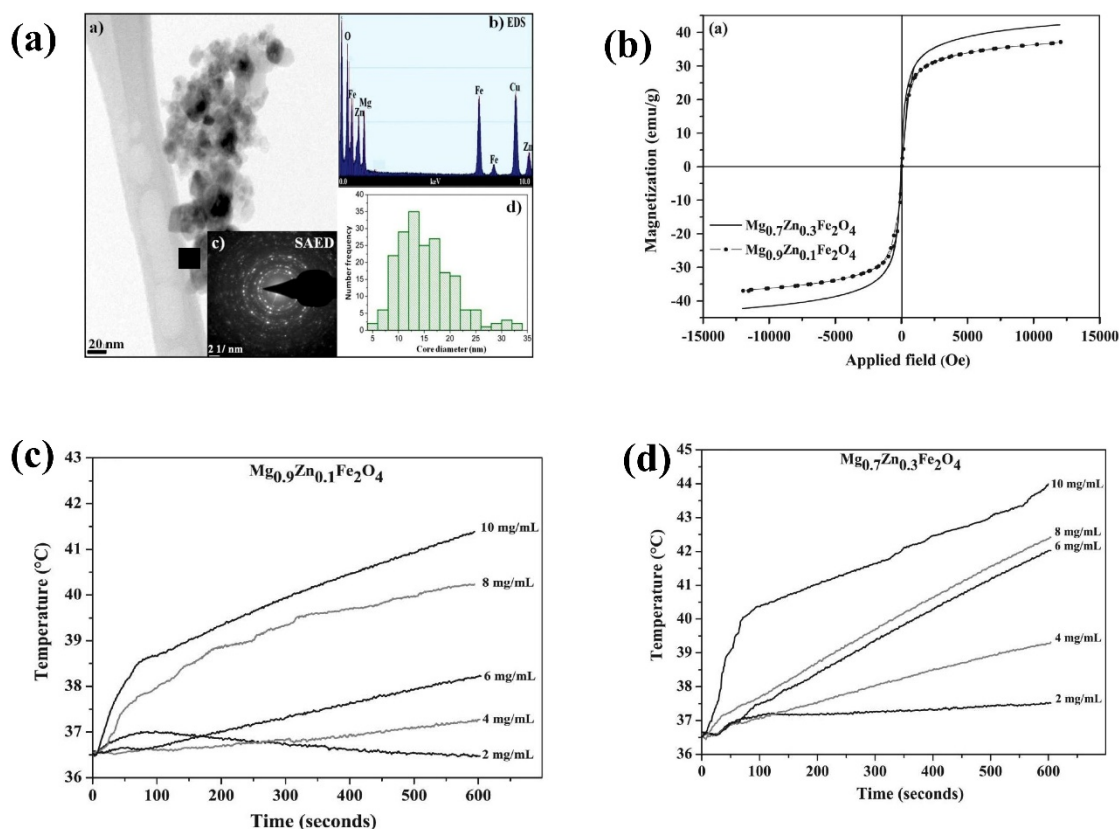
Figure 21. (a) TEM image of the Mg doped ZFNPs insets showing SAED (selected area electron diffraction) pattern, EDX (energy dispersive X-ray spectroscopy) pattern and bar graph of particle size distribution. (b) The plot of magnetization vs applied magnetic field for different compositions of Mg doped Zinc Ferrites. (c) The heating profile of $Mg_{0.9}Zn_{0.1}Fe_2O_4$ nanoparticle fluids of different concentrations. (d) The heating profile of $Mg_{0.7}Zn_{0.3}Fe_2O_4$ nanoparticle fluids of different concentrations. (Reproduced with permissions from ref.[135]. Copyright 2016. ELSEVIER).

Another very attractive doped system is Mg doped zinc ferrite, one of the potential systems with hyperthermia characteristics that has seen limited research. To the best of our knowledge, we found only three published articles that used Mg doped ZFNPs for hyperthermia applications.[133–135] The most important advantage of this system is that both zinc and magnesium are present in the human blood stream in considerably larger amounts than the other transition metals. Their presence is also known to reduce the chances and risks of several types of carcinomas. Thus, even if trace amounts of the NPs are left inside the system, they would not be as harmful as other transition metal doped systems. These NPs have a low cytotoxicity and a high biocompatibility. The most recent study on Mg doped Zinc ferrites for hyperthermia was conducted by Rodriguez et al.[135], who synthesized Mg doped ZFNPs using a sol gel method.

The TEM image obtained for these particles is shown in **Figure 21. (a)**. The average diameter of these NPs was found to be approximately 12 nm. These researchers synthesized several

compositions using varying Zn and Mg doping ratios, the compositions exhibiting good saturation magnetization response including $Mg_{0.9}Zn_{0.1}Fe_2O_4$ and $Mg_{0.7}Zn_{0.3}Fe_2O_4$. The magnetization response with an applied magnetic field is shown in **Figure 21. (b)**. The hyperthermia characteristics were recorded using a magnetic field of 10.2 kA/m and a frequency of 326 kHz. The ferrofluids were prepared for these two compositions from 2 mg/mL to 10 mg/ml. The temperature time profiles of these compositions are shown in **Figure 21. (c) and (d),** respectively. The $Mg_{0.7}Zn_{0.3}Fe_2O_4$ composition showed better hyperthermia response, its therapeutic range being achieved in approximately 10 mins for the 10 mg/mL concentration ferrofluid. These NPs show potential for mild hyperthermia applications. Their primary limitation is their low saturation magnetization, which, similar to the systems discussed here, can be improved using better synthesis methods and coating materials. A second challenge lies in their high Curie temperature. In their recent article, Alghamdi et al.[136] have shown that by tuning the zinc magnesium doping ratio, the Curie temperature can be manipulated

and lowered. Perhaps better exploration in this direction would result in a self-regulated hyperthermia agent. The Mg doped ZFNPs have significant potential, and this system offers plenty of opportunities.

Table 6. : Ni-Zn ferrite nanostructures s and their critical parameters for MHT applications

Material	Coating	Morphology	Particle Size (nm)	M_s (emu/g)	SAR (W/g)	H (KA/m)	f (kHz)	T_{Max} (°C)	t_{exp} (min)	t_{42} (min)	Ref
$Ni_{0.6}Zn_{0.35}Fe_{2.05}O_4$	Citric Acid	Spherical clusters	4.4	36.3	131.5	15.91	746	51	50	13	[126]
$Ni_{0.5}Zn_{0.5}Fe_2O_4$	Oleic Acid Oleylamine	Spherical	11	66.74	410	35.28	316	53	12	5	[128]
$Ni_{0.65}Zn_{0.35}Fe_2O_4$	PEG	Spherical	8.5	55	33	4.4	260	50	20	10	[129]
$Ni_{0.8}Zn_{0.2}Fe_2O_4$	TREG (triethylene glycol)	Spherical	18.73	72.4	98	4.4	216	72	23	2	[137]

8. Concluding Remarks and Outlook

In this review, we have primarily analyzed the hyperthermic performance of zinc ferrite nanostructures beginning from spherical morphologies to anisotropic systems involving pure zinc ferrite as well as several doped and composite nano systems. It has been observed that anisotropic zinc ferrite exhibits improved magnetic properties and MHT performance compared to the spherical counterparts. In addition to its biocompatibility and magnetic properties, the primary advantage of zinc ferrite is its ability to transform into a paramagnetic substance at temperatures within the range of the MHT therapeutic window. This quality provides zinc ferrite-based systems (as primarily observed for Co-Zn ferrite nanoparticles) a self-regulated temperature (Curie temperature) or an auto cut-off near ~ 43-46 °C, which is an essential pre-requisite for clinical hyperthermia applications. Not many studies involving *in vivo* or pre-clinical studies based on mice models have used zinc ferrite-based nanoparticles. Currently, Mn-Zn ferrite is the nanomaterial receiving the most research attention in pre-clinical applications. Considering the potency of these nano systems, systematic *in vivo* studies on several other doped zinc ferrite-based nanostructures exhibiting different morphologies need to be conducted to exploit these materials in advanced biomedical applications including MHT, targeted drug delivery and magnetic resonance imaging (MRI). Furthermore, detailed studies must be conducted covering the fundamental nanomagnetic aspects of zinc ferrite-based nanoparticles, including research on interparticle dipolar interactions,[138–140] magnetic spin relaxation dynamics[141–146] and

exchange-bias effects[147–150] targeting spherical and anisotropic morphologies of both pure and doped/composite systems. A rigorous understanding of these fundamental nanophysics aspects could possibly help us in designing much sophisticated zinc ferrite-based nanosystems for future applications.

Most of the scientific literature comprises studies focused on transition-metal doped zinc ferrite systems; however, the impact of doping rare-earth ions into the spinel structure of zinc ferrite is yet to be understood. Limited studies have investigated the impact of rare-earth doping on zinc ferrite. It would be interesting to see how rare-earth doping, particularly MRI active ions like Gd^{3+} and Dy^{3+}, influence the morphology, magnetic properties, and Curie temperature of zinc ferrite. Introducing rare-earth ions into zinc-ferrite could possibly equip these nanomaterials with multi-functional applications in terms of both MHT and T_1-T_2 dual modal MRI. In addition, in the field of nanorobotics for biomedical applications, it has been reported that a zinc ferrite coating on the helical surfaces of the robots stabilizes them against magnetic agglomeration and simultaneously registers a reasonably good hyperthermia performance,[151] suggesting the need for further exploration of the functionalization of these nanorobots with Mn-Zn ferrite and rare-earth doped zinc ferrite nanosystems for potential utilization of these helices in cancer theranostics, including MHT and MRI. Moreover, zinc ferrite is considered a prime candidate for non-invasive glucose monitoring[152] and photocatalytic dye degradation purposes[153]; therefore, more systematic studies that increase our understanding of these nanosystems could result in zinc ferrite

becoming a future nanomaterial for both biomedical and environmental applications.

Author Contributions

All authors participated in discussions and proofread the manuscript. PS and PC contributed equally to this work.

Conflicts of interest

The authors declare no conflict of interest.

Acknowledgements

References

1   J. D. Q A Pankhurst, J Connolly, SKJones, *J. Phys. D. Appl. Phys.*, 2003, **36**, 591–626.

2   D. L. Leslie-Pelecky and R. D. Rieke, *Chem. Mater.*, 1996, **8**, 1770–1783.

3   S. P. Gubin, *Magnetic nanoparticles*, John Wiley & Sons, 2009.

4   C. C. Berry, *J. Phys. D. Appl. Phys.*, 2009, **42**, 224003.

5   A. K. Gupta and M. Gupta, *Biomaterials*, 2005, **26**, 3995–4021.

6   T. Ibelli, S. Templeton and N. Levi-Polyachenko, *Int. J. Hyperth.*, 2018, **34**, 144–156.

7   L. A. Thomas, L. Dekker, M. Kallumadil, P. Southern, M. Wilson, S. P. Nair, Q. A. Pankhurst and I. P. Parkin, *J. Mater. Chem.*, 2009, **19**, 6529–6535.

8   X. Liu, N. Song, D. Qian, S. Gu, J. Pu, L. Huang, J. Liu and K. Qian, *ACS Biomater. Sci. Eng.*, 2022, **8**, 4092–4109.

9   J. W. Phillips, A. Prominski and B. Tian, *VIEW*, 2022, **3**, 20200157.

10   D. Zheng, K. Yang and Z. Nie, *VIEW*, 2021, **2**, 20200067.

11   R. K. GILCHRIST, R. MEDAL, W. D. SHOREY, R. C. HANSELMAN, J. C. PARROTT and C. B. TAYLOR, *Ann. Surg.*, 1957, **146**, 596–606.

12   A. Hoter, A. O. Alsantely, E. Alsharaeh, G. Kulik and I. M. Saadeldin, in *Heat Shock Proteins*, 2020, pp. 53–78.

13   J. Pan, Y. Xu, Q. Wu, P. Hu and J. Shi, *J. Am. Chem. Soc.*, 2021, **143**, 8116–8128.

14   T. A. Meyer, C. Zhang, G. Bao and Y. Ke, *Nano Lett.*, 2020, **20**, 2799–2805.

15   A. Włodarczyk, S. Gorgoń, A. Radoń and K. Bajdak-Rusinek, *Nanomaterials*, 2022, **12**, 1807.

16   N. G. Shetake, M. Ali, A. Kumar, J. Bellare and B. N. Pandey, *Biomater. Adv.*, 2022, **142**, 213147.

17   B. Issa, I. M. Obaidat, B. A. Albiss and Y. Haik, *Int. J. Mol. Sci.*, 2013, **14**, 21266–21305.

18   M. Vassallo, D. Martella, G. Barrera, F. Celegato, M. Coïsson, R. Ferrero, E. S. Olivetti, A. Troia, H. Sözeri, C. Parmeggiani, D. S. Wiersma, P. Tiberto and A. Manzin, *ACS Omega*, 2023, **8**, 2143–2154.

19   A. G. Díez, M. Rincón-Iglesias, S. Lanceros-Méndez, J. Reguera and E. Lizundia, *Mater. Today Chem.*, 2022, **26**, 101220.

20   S. M. Dadfar, D. Camozzi, M. Darguzyte, K. Roemhild, P. Varvarà, J. Metselaar, S. Banala, M. Straub, N. Güvener, U. Engelmann, I. Slabu, M. Buhl, J. van Leusen, P. Kögerler, B. Hermanns-Sachweh, V. Schulz, F. Kiessling and T. Lammers, *J. Nanobiotechnology*, 2020, **18**, 22.

21   N. Jović Orsini, M. M. Milić and T. E. Torres, *Nanotechnology*, 2020, **31**, 225707.

22   S. B. Somvanshi, R. V. Kumar, J. S. Kounsalye, T. S. Saraf and K. M. Jadhav, *AIP Conf. Proc.*, 2019, **2115**, 30522.

23   Darwish, Kim, Lee, Ryu, Lee and Yoon, *Nanomaterials*, 2019, **9**, 1176.

24   H. Gavilán, S. K. Avugadda, T. Fernández-Cabada, N. Soni, M. Cassani, B. T. Mai, R. Chantrell and T. Pellegrino, *Chem. Soc. Rev.*, 2021, **50**, 11614–11667.

25   Y. Song, D. Li, Y. Lu, K. Jiang, Y. Yang, Y. Xu, L. Dong, X. Yan, D. Ling, X. Yang and S.-H. Yu, *Natl. Sci. Rev.*, 2020, **7**, 723–736.

26   A. Nishikawa, Y. Suzuki, M. Kaneko and A. Ito, *Cancer Immunol. Immunother.*, 2023, **72**, 1493–1504.

27   R. Gupta and D. Sharma, *ACS Chem. Neurosci.*, 2019, **10**, 1157–1172.

28   K. Maier-Hauff, F. Ulrich, D. Nestler, H. Niehoff, P. Wust, B.

Thiesen, H. Orawa, V. Budach and A. Jordan, *J. Neurooncol.*, 2011, **103**, 317–324.

29   M. Barani, A. Rahdar, M. Mukhtar, S. Razzaq, M. Qindeel, S. A. Hosseini Olam, A. C. Paiva-Santos, N. Ajalli, S. Sargazi, D. Balakrishnan, A. K. Gupta and S. Pandey, *Mater. Today Chem.*, 2022, **26**, 101131.

30   S. S. Laha, N. D. Thorat, G. Singh, C. I. Sathish, J. Yi, A. Dixit and A. Vinu, *Small*, 2022, **18**, 2104855.

31   G. Rana, P. Dhiman, A. Kumar, D.-V. N. Vo, G. Sharma, S. Sharma and M. Naushad, *Chem. Eng. Res. Des.*, 2021, **175**, 182–208.

32   C. R. Kalaiselvan, S. S. Laha, S. B. Somvanshi, T. A. Tabish, N. D. Thorat and N. K. Sahu, *Coord. Chem. Rev.*, 2022, **473**, 214809.

33   D. Lachowicz, W. Górka, A. Kmita, A. Bernasik, J. Żukrowski, W. Szczerba, M. Sikora, C. Kapusta and S. Zapotoczny, *J. Mater. Chem. B*, 2019, **7**, 2962–2973.

34   Y. Hadadian, A. P. Ramos and T. Z. Pavan, *Sci. Rep.*, 2019, **9**, 1–14.

35   H. A. Alhadlaq, M. J. Akhtar and M. Ahamed, *Cell Biosci.*, 2015, **5**, 55.

36   S. B. Somvanshi, P. B. Kharat, M. V. Khedkar and K. M. Jadhav, *Ceram. Int.*, 2020, **46**, 7642–7653.

37   L. Raghavan, G. Pookat, H. Thomas, S. Ojha, D. K. Avasthi and M. R. Anantharaman, *J. Magn. Magn. Mater.*, 2015, **385**, 265–271.

38   N. Li, G. Huang, H. Xiao, Q. Feng and S. Fu, *Carbon N. Y.*, 2019, **144**, 216–227.

39   B. Aslibeiki and P. Kameli, *J. Magn. Magn. Mater.*, 2015, **385**, 308–312.

40   G. B. Ji, S. L. Tang, S. K. Ren, F. M. Zhang, B. X. Gu and Y. W. Du, *J. Cryst. Growth*, 2004, **270**, 156–161.

41   P. Appa Rao, K. Srinivasa Rao, T. R. K. Pydi Raju, G. Kapusetti, M. Choppadandi, M. Chaitanya Varma and K. H. Rao, *J. Alloys Compd.*, 2019, **794**, 60–67.

42   W. Zhang, C. Wu and S. R. P. Silva, *Expert Rev. Anticancer Ther.*, 2018, **18**, 723–725.

43   R. Arulmurugan, B. Jeyadevan, G. Vaidyanathan and S. Sendhilnathan, *J. Magn. Magn. Mater.*, 2005, **288**, 470–477.

44   M. Ognjanović, D. M. Stanković, Y. Ming, H. Zhang, B. Jančar, B. Dojčinović, Ž. Prijović and B. Antić, *J. Alloys Compd.*, 2019, **777**, 454–462.

45   S. Shatooti, M. Mozaffari, G. Reiter, D. Zahn and S. Dutz, *Phys. B Condens. Matter*, 2022, **625**, 413468.

46   M. K. Lima-Tenório, E. T. Tenório-Neto, A. A. W. Hechenleitner, H. Fessi and E. A. G. Pineda, *J. Colloid Sci. Biotechnol.*, 2016, **5**, 45–54.

47   Rachna, N. B. Singh and A. Agarwal, *Mater. Today Proc.*, 2018, **5**, 9148–9155.

48   R. M. Borade, S. B. Somvanshi, S. B. Kale, R. P. Pawar and K. M. Jadhav, *Mater. Res. Express*, 2020, **7**, 016116.

49   G. M. Alzoubi, *J. Supercond. Nov. Magn.*, 2022, **35**, 2417–2424.

50   B. Behdadfar, A. Kermanpur, H. Sadeghi-Aliabadi, M. D. P. Morales and M. Mozaffari, *J. Magn. Magn. Mater.*, 2012, **324**, 2211–2217.

51   J. Jang, H. Nah, J.-H. Lee, S. H. Moon, M. G. Kim and J. Cheon, *Angew. Chemie Int. Ed.*, 2009, **48**, 1234–1238.

52   A. Pardo, B. Pelaz, J. Gallo, M. Bañobre-López, W. J. Parak, S. Barbosa, P. Del Pino and P. Taboada, *Chem. Mater.*, 2020, **32**, 2220–2231.

53   O. A. Onyedikachi, S. O. Aisida, A. Agbogu, I. Rufus, I. Ahmad, M. Maaza and F. I. Ezema, *Appl. Phys. A Mater. Sci. Process.*, 2022, **128**, 1–9.

54   E. Céspedes, J. M. Byrne, N. Farrow, S. Moise, V. S. Coker, M. Bencsik, J. R. Lloyd and N. D. Telling, *Nanoscale*, 2014, **6**, 12958–12970.

55   S. O. Aisida, A. Ali, O. E. Oyewande, I. Ahmad, A. Ul-Hamid, T. Zhao, M. Maaza and F. I. Ezema, *J. Nanoparticle Res.*, 2021, **23**, 47.

56   K. Sathiyamurthy, C. Rajeevgandhi, S. Bharanidharan, P. Sugumar and S. Subashchandrabose, *Chem. Data Collect.*, 2020, **28**, 100477.

57   S. Sugi, S. Radhika and C. M. Padma, *Mater. Chem. Phys.*, 2022, **292**, 126799.

58   M. Ebrahimi, R. Raeisi Shahraki, S. A. Seyyed Ebrahimi and S. M. Masoudpanah, *J. Supercond. Nov. Magn.*, 2014, **27**, 1587–1592.

59   D. D. Andhare, S. A. Jadhav, M. V. Khedkar, S. B. Somvanshi, S. D. More and K. M. Jadhav, *J. Phys. Conf. Ser.*, 2020, **1644**, 012014.

60   P. Puspitasari, U. A. Rizkia, S. Sukarni, A. A. Permanasari, A. Taufiq and A. B. N. R. Putra, *Mater. Res.*, 2021, **24**, 2–6.

61   R. Raeisi Shahraki, M. Ebrahimi, S. A. Seyyed Ebrahimi and S. M. Masoudpanah, *J. Magn. Magn. Mater.*, 2012, **324**,

3762–3765.

62 L. T. T. Nguyen, K. D. M. Nguyen, T. A. Nguyen and K. No, *Ceram. Int.*, 2022, **48**, 4090–4095.

63 M. A. Ait Kerroum, A. Essyed, C. Iacovita, W. Baaziz, D. Ihiawakrim, O. Mounkachi, M. Hamedoun, A. Benyoussef, M. Benaissa and O. Ersen, *J. Magn. Magn. Mater.*, 2019, **478**, 239–246.

64 S. O. Aisida, P. A. Akpa, I. Ahmad, M. Maaza and F. I. Ezema, *Phys. B Condens. Matter*, 2019, **571**, 130–136.

65 E. S. Lima, L. S. Costa, G. R. L. M. Sampaio, E. S. Oliveira, E. B. Silva, H. O. Nascimento, R. F. Nascimento, K. O. Moura, M. Bastos-Neto, A. R. Loiola and J. M. Sasaki, *J. Braz. Chem. Soc.*, 2019, **30**, 882–891.

66 R. P. Sharma, S. D. Raut, V. V Jadhav, A. S. Kadam and R. S. Mane, *Mater. Lett.*, 2019, **237**, 165–167.

67 S. B. Patil, H. S. B. Naik, G. Nagaraju, R. Viswanath, S. K. Rashmi and M. Vijay, *Mater. Chem. Phys.*, 2018, **212**, 351–362.

68 M. H. Mahmoud, A. M. Hassan, A. E. A. Said and T. A. Taha, *Inorg. Chem. Commun.*, 2022, **144**, 109932.

69 P. Sivakumar, K. Thyagarajan and A. G. Kumar, *Dig. J. Nanomater. Biostructures*, 2018, **13**, 1117–1122.

70 X. Cao, *Nano Express*, 2021, **2**, 024001.

71 I. Castellanos-Rubio, O. Arriortua, L. Marcano, I. Rodrigo, D. Iglesias-Rojas, A. Barón, A. Olazagoitia-Garmendia, L. Olivi, F. Plazaola, M. L. Fdez-Gubieda, A. Castellanos-Rubio, J. S. Garitaonandia, I. Orue and M. Insausti, *Chem. Mater.*, 2021, **33**, 3139–3154.

72 D. O. Okoroh, S. O. Aisida and P. U. Asogwa, 2018, **10**, 52–56.

73 D. Tomar and P. Jeevanandam, *J. Magn. Magn. Mater.*, 2022, **564**, 170033.

74 L. Kubíčková, J. Koktan, T. Kořínková, M. Klementová and T. Kmječ, *J. Magn. Magn. Mater.*, 2020, **498**, 166083.

75 L. Andjelkovi, Š. Marija, M. Laki, D. Jeremi and P. Vuli, *Ceram. Int.*, 2018, **44**, 14163–14168.

76 L. Yang, C. Sun, H. Lin, X. Gong, T. Zhou, W. Deng, Z. Chen and J. Gao, *Chem. Mater.*, 2019, **31**, 1381–1390.

77 S. Bram, M. N. Gordon, M. A. Carbonell, M. Pink, B. D. Stein, D. G. Morgan, D. Aguila, G. Arom, S. E. Skrabalak, Y. Losovyj and L. M. Bronstein, *ACS Omega*, 2018, **3**, 16328–16337.

78 A. Kmita, D. Lachowicz, J. Żukrowski, M. Gajewska, W.

Szczerba, J. Kuciakowski, S. Zapotoczny and M. Sikora, *Materials (Basel).*, 2019, **12**, 1048.

79 T. Zargar, A. Kermanpur, S. Labbaf, A. B. Houreh and M. H. N. Esfahani, *Mater. Chem. Phys.*, 2018, **212**, 432–439.

80 T. Zargar and A. Kermanpur, *Ceram. Int.*, 2017, **43**, 5794–5804.

81 C. Hasirci, O. Karaagac and H. Köçkar, *J. Magn. Magn. Mater.*, 2019, **474**, 282–286.

82 A. R. Al-areqi, X. Yu, R. Yang, C. Wang, C. Wu and W. Zhang, *J. Magn. Magn. Mater.*, 2023, **579**, 170839.

83 S. Dabagh, S. A. Haris and Y. N. Ertas, *ACS Biomater. Sci. Eng.*, 2023, **9**, 4138–4148.

84 M. V. Shisode, J. S. Kounsalye, A. V. Humbe, R. C. Kambale and K. M. Jadhav, *Appl. Phys. A Mater. Sci. Process.*, 2018, **124**, 1–11.

85 V. D. Kassabova-zhetcheva, L. P. Pavlova, B. I. Samuneva, Z. P. Cherkezova-zheleva, I. G. Mitov and M. T. Mikhov, 2007, **5**, 107–117.

86 NIH office of diatery suppliments, Zinc Fact Sheet for Health Professionals.

87 S. Chakraborty, D. Menon, V. S. Akhil Varri, M. Sahoo, R. Ranganathan, P. Zhang and S. K. Misra, *Environ. Sci. Nano*, 2023, **10**, 1553–1569.

88 V. Vijayakanth, V. Vinodhini, A. Aparna, M. S. Malavika and C. Krishnamoorthi, *J. Mater. Sci. Mater. Electron.*, 2021, **32**, 2395–2408.

89 A. Pardo, S. Yáñez, Y. Piñeiro, R. Iglesias-Rey, A. Al-Modlej, S. Barbosa, J. Rivas and P. Taboada, *ACS Appl. Mater. Interfaces*, 2020, **12**, 9017–9031.

90 A. Muela, D. Muñoz, R. Martín-Rodríguez, I. Orue, E. Garaio, A. Abad Díaz De Cerio, J. Alonso, J. Á. García and M. L. Fdez-Gubieda, *J. Phys. Chem. C*, 2016, **120**, 24437–24448.

91 Y. Yang, X. Liu, Y. Yang, W. Xiao, Z. Li, D. Xue, F. Li and J. Ding, *J. Mater. Chem. C*, 2013, **1**, 2875–2885.

92 F. H. L. Starsich, G. A. Sotiriou, M. C. Wurnig, C. Eberhardt, A. M. Hirt, A. Boss and S. E. Pratsinis, *Adv. Healthc. Mater.*, 2016, **5**, 2698–2706.

93 S. He, H. Zhang, Y. Liu, F. Sun, X. Yu, X. Li, L. Zhang, L. Wang, K. Mao, G. Wang, Y. Lin, Z. Han, R. Sabirianov and H. Zeng, *Small*, 2018, **14**, 1800135.

94 A. Hanini, L. Lartigue, J. Gavard, K. Kacem, C. Wilhelm, F. Gazeau, F. Chau and S. Ammar, *J. Magn. Magn. Mater.*,

2016, **416**, 315–320.

95   S. Sabale, V. Jadhav, V. Khot, X. Zhu, M. Xin and H. Chen, *J. Mater. Sci. Mater. Med.*, 2015, **26**, 127.

96   A. M. C. Krishnamoorthi, K. C. Babu and N. C. Pavithra, *Appl. Phys. A*, 2019, **125**, 1–10.

97   L. B. de Mello, L. C. Varanda, F. A. Sigoli and I. O. Mazali, *J. Alloys Compd.*, 2019, **779**, 698–705.

98   L. Wang, S.-M. Lai, C.-Z. Li, H.-P. Yu, P. Venkatesan and P.-S. Lai, *Pharmaceutics*, 2022, **14**, 1000.

99   T. Kaewmanee, S. Wannapop, A. Phuruangrat, T. Thongtem, O. Wiranwetchayan, W. Promnopas, S. Sansongsiri and S. Thongtem, *Inorg. Chem. Commun.*, 2019, **103**, 87–92.

100   S. O. Aisida, M. H. Alnasir, S. Botha, A. K. H. Bashir, R. Bucher, I. Ahmad, T. kai Zhao, M. Maaza and F. I. Ezema, *Eur. Polym. J.*, 2020, **132**, 109739.

101   Y. Wang, L. Zou, Z. Qiang, J. Jiang, Z. Zhu and J. Ren, *ACS Biomater. Sci. Eng.*, 2020, **6**, 3550–3562.

102   J. Xie, Y. Zhang, C. Yan, L. Song, S. Wen, F. Zang, G. Chen, Q. Ding, C. Yan and N. Gu, *Biomaterials*, 2014, **35**, 9126–9136.

103   J. Stergar, Z. Jirák, P. Veverka, L. Kubíčková, T. Vrba, J. Kuličková, K. Knížek, F. Porcher, J. Kohout and O. Kaman, *J. Magn. Magn. Mater.*, 2019, **475**, 429–435.

104   L. M. Slavu, R. Rinaldi and R. Di Corato, *Appl. Sci.*, 2021, **11**, 11183.

105   J. Jang, H. Nah, J.-H. Lee, S. H. Moon, M. G. Kim and J. Cheon, *Angew. Chemie*, 2009, **121**, 1260–1264.

106   C. Wang, N. Zhao, Y. Huang, R. He, S. Xu and W. Yuan, *Chem. Eng. J.*, 2020, **401**, 126100.

107   R. D. Raland and J. P. Borah, *J. Phys. D. Appl. Phys.*, 2017, **50**, 035001.

108   L. B. de Mello, L. C. Varanda, F. A. Sigoli and I. O. Mazali, *J. Alloys Compd.*, 2019, **779**, 698–705.

109   Y. Qu, J. Li, J. Ren, J. Leng, C. Lin and D. Shi, *ACS Appl. Mater. Interfaces*, 2014, **6**, 16867–16879.

110   J. Li, Y. Qu, J. Ren, W. Yuan and D. Shi, *Nanotechnology*, 2012, **23**, 505706.

111   I. Sharifi and H. Shokrollahi, *J. Magn. Magn. Mater.*, 2012, **324**, 2397–2403.

112   G. V Duong, R. S. Turtelli, W. C. Nunes, E. Schafler, N. Hanh, R. Grössinger and M. Knobel, *J. Non. Cryst. Solids*, 2007, **353**, 805–807.

113   G. Vaidyanathan and S. Sendhilnathan, *Phys. B Condens. Matter*, 2008, **403**, 2157–2167.

114   G. V Duong, N. Hanh, D. V Linh, R. Groessinger, P. Weinberger, E. Schafler and M. Zehetbauer, *J. Magn. Magn. Mater.*, 2007, **311**, 46–50.

115   D. S. Nikam, S. V Jadhav, V. M. Khot, M. R. Phadatare and S. H. Pawar, *J. Magn. Magn. Mater.*, 2014, **349**, 208–213.

116   L. Kumar, P. Kumar and M. Kar, *J. Alloys Compd.*, 2013, **551**, 72–81.

117   D. D. Andhare, S. R. Patade, M. V. Khedkar, A. A. Nawpute and K. M. Jadhav, *Appl. Phys. A*, 2022, **128**, 1–12.

118   S. Kumari, M. K. Manglam, L. Kumar, P. Seal, J. P. Borah, M. Kumar Zope and M. Kar, *J. Sol-Gel Sci. Technol.*, 2022, **101**, 546–561.

119   T. Tatarchuk, A. Shyichuk, Z. Sojka, J. Gryboś, M. Naushad, V. Kotsyubynsky, M. Kowalska, S. Kwiatkowska-Marks and N. Danyliuk, *J. Mol. Liq.*, 2021, **328**, 115375.

120   H. Ghayour, M. Abdellahi, M. G. Nejad, A. Khandan and S. Saber-Samandari, *J. Aust. Ceram. Soc.*, 2018, **54**, 223–230.

121   R. A. Bohara, N. D. Thorat, A. K. Chaurasia and S. H. Pawar, *RSC Adv.*, 2015, **5**, 47225–47234.

122   C. Gómez-Polo, V. Recarte, L. Cervera, J. J. Beato-López, J. López-García, J. A. Rodríguez-Velamazán, M. D. Ugarte, E. C. Mendonça and J. G. S. Duque, *J. Magn. Magn. Mater.*, 2018, **465**, 211–219.

123   H. Choi, S. Lee, T. Kouh, S. J. Kim, C. S. Kim and E. Hahn, *J. Korean Phys. Soc.*, 2017, **70**, 89–92.

124   M. Veverka, K. Závěta, O. Kaman, P. Veverka, K. Knížek, E. Pollert, M. Burian and P. Kašpar, *J. Phys. D. Appl. Phys.*, 2014, **47**, 065503.

125   S. W. Lee and C. S. Kim, *J. Magn. Magn. Mater.*, 2006, **304**, 418–420.

126   P. V. Ramana, K. S. Rao, K. R. Kumar, G. Kapusetti, M. Choppadandi, J. N. Kiran and K. H. Rao, *Mater. Chem. Phys.*, 2021, **266**, 124546.

127   R. D. R. Kahmei, P. Seal and J. P. Borah, *Nanoscale Adv.*, 2021, **3**, 5339–5347.

128   A. Manohar, K. Chintagumpala and K. H. Kim, *Ceram. Int.*, 2021, **47**, 7052–7061.

129   A. Ahmad, H. Bae, I. Rhee and S. Hong, *J. Korean Phys. Soc.*, 2017, **70**, 615–620.

130   A. I. Tovstolytkin, M. M. Kulyk, V. M. Kalita, S. M. Ryabchenko, V. O. Zamorskyi, O. P. Fedorchuk, S. O.

Solopan and A. G. Belous, *J. Magn. Magn. Mater.*, 2019, **473**, 422–427.

131   A. Ahmad, H. Bae, I. Rhee and S. Hong, *J. Magn. Magn. Mater.*, 2018, **447**, 42–47.

132   B. T. Naughton and D. R. Clarke, *J. Am. Ceram. Soc.*, 2007, **90**, 3541–3546.

133   H. Liu, A. Li, X. Ding, F. Yang and K. Sun, *Solid State Sci.*, 2019, **93**, 101–108.

134   H. M. El-Sayed, I. A. Ali, A. Azzam and A. A. Sattar, *J. Magn. Magn. Mater.*, 2017, **424**, 226–232.

135   P. Y. Reyes-Rodríguez, D. A. Cortés-hernández, J. C. Escobedo-bocardo, J. M. Almanza-robles, H. J. Sánchez-fuentes, L. E. De León-prado, J. Méndez-nonell and G. F. Hurtado-lópez, *J. Magn. Magn. Mater.*, 2017, **427**, 268–271.

136   N. Alghamdi, J. Stroud, M. Przybylski and J. Żukrowski, *J. Magn. Magn. Mater.*, 2020, **497**, 165981.

137   A. Ahmad, H. Bae, I. Rhee and S. Hong, *J. Magn. Magn. Mater.*, 2018, **447**, 42–47.

138   C. J. Bae, S. Angappane, J.-G. Park, Y. Lee, J. Lee, K. An and T. Hyeon, *Appl. Phys. Lett.*, 2007, **91**, 102502.

139   S. S. Laha, R. J. Tackett and G. Lawes, *Phys. B Condens. Matter*, 2014, **448**, 69–72.

140   K. Wu, D. Su, R. Saha, J. Liu and J.-P. Wang, *J. Phys. D. Appl. Phys.*, 2019, **52**, 335002.

141   K. Nadeem, H. Krenn, T. Traussing and I. Letofsky-Papst, *J. Appl. Phys.*, 2011, **109**, 13912.

142   S. S. Laha, R. Regmi and G. Lawes, *J. Phys. D. Appl. Phys.*, 2013, **46**, 325004.

143   B. Aslibeiki, P. Kameli, H. Salamati, M. Eshraghi and T. Tahmasebi, *J. Magn. Magn. Mater.*, 2010, **322**, 2929–2934.

144   S. S. Laha, E. Abdelhamid, M. P. Arachchige, A. Kumar and A. Dixit, *J. Am. Ceram. Soc.*, 2017, **100**, 1534–1541.

145   R. J. Tackett, J. G. Parsons, B. I. Machado, S. M. Gaytan, L. E. Murr and C. E. Botez, *Nanotechnology*, 2010, **21**, 365703.

146   C. E. Botez, A. H. Adair and R. J. Tackett, *J. Phys. Condens. Matter*, 2015, **27**, 0–6.

147   E. Abdelhamid, S. S. Laha, A. Dixit, G. A. Nazri, O. D. Jayakumar and B. Nadgorny, *J. Electron. Mater.*, 2019, **48**, 3297–3303.

148   J. Nogués, J. Sort, V. Langlais, V. Skumryev, S. Suriñach, J. S. Muñoz and M. D. Baró, *Phys. Rep.*, 2005, **422**, 65–117.

149   S. P. Tsopoe, C. Borgohain, R. Fopase, L. M. Pandey and J. P. Borah, *Sci. Rep.*, 2020, **10**, 18666.

150   S.-S. Tan, N. Wang, C.-Q. Yang, L. Wang, Y. Hu, J. Li, S.-C. Xu, M. Lu and H.-B. Li, *J. Magn. Magn. Mater.*, 2022, **556**, 169428.

151   P. L. Venugopalan, S. Jain, S. Shivashankar and A. Ghosh, *Nanoscale*, 2018, **10**, 2327–2332.

152   S. Laha, A. Rajput, S. S. Laha and R. Jadhav, *Biosensors*, 2022, **12**, 1–20.

153   Sonu, S. Sharma, V. Dutta, P. Raizada, A. Hosseini-Bandegharaei, V. Thakur, V.-H. Nguyen, Q. VanLe and P. Singh, *J. Environ. Chem. Eng.*, 2021, **9**, 105812.